Master's Theses   Master's Theses and Graduate Research

Fall 2016

SERS Intensity Correlations to LSPR on Aggregated Au@Ag Systems

Caesar Alexander Munera
San Jose State University

Follow this and additional works at: https://scholarworks.sjsu.edu/etd_theses

SERS INTENSITY CORRELATIONS TO
LSPR ON AGGREGATED Au@Ag SYSTEMS

A Thesis

Presented to

The Faculty of the Department of Chemistry

San José State University

In Partial Fulfillment

of the Requirement for the Degree

Master of Science

By

Caesar A. Múnera

December 2016

The Designated Thesis Committee Approves the Thesis Titled

SERS INTENSITY CORRELATIONS TO
LSPR ON AGGREGATED Au@Ag SYSTEMS

by

Caesar A. Múnera

APPROVED FOR THE DEPARTMENT OF CHEMISTRY

SAN JOSÉ STATE UNIVERSITY

December 2016

Roger H. Terrill, Ph.D.	Department of Chemistry
Joseph J. Pesek, Ph.D.	Department of Chemistry
David J.R. Brook, Ph.D.	Department of Chemistry

ABSTRACT

SERS INTENSITY CORRELATIONS TO LSPR
ON AGGREGATED Au@Ag SYSTEMS

by Caesar A. Múnera

The optimal surface enhanced Raman scattering (SERS) intensity was correlated

to the localized surface plasmon resonance (LSPR) of individual and aggregated gold

core/silver shell (*Au@Ag*) nanoparticles (NPs) in titrations involving the addition of both

SERS label (e.g., rhodamine 6G, R6G) and the non-SERS active aggregant (chemical

species that triggers the aggregation of NPs) potassium chloride (KCl). Titrating NP

solutions with pure SERS label has often resulted in highly non-linear calibrations. In

some cases, addition of non-SERS active aggregating agents such as KCl has also

resulted in a large increase in SERS signals. An order of initial addition was followed in

this report to find any advantage from the initial addition between the SERS label or the

aggregant KCl. Interactions between Au@Ag solution and the SERS labels of R6G,

4-mercaptopyridine (MPY) and 4-mercaptobenzoic acid (MBA) were followed using

spectrophotometric titrations. Evaluations of the role of aggregation in NP solutions

were conducted through the micro-titrations using a quartz cuvette and in two separate

stages: (1) a single amount of KCl was followed by increasing amounts of SERS label,

and (2) a single amount of SERS label was followed by increasing amounts of KCl. The

present reports allowed to conclude that the graphs of SERS intensity (λ_{EX} = 785nm,

corrected for solution absorption) versus aggregate absorptions (λ_{AG} = 830 nm) had a

correlation between intense SERS and LSPR band extinctions.

ACKNOWLEDGMENTS

TABLE OF CONTENTS

LIST OF TABLES

LIST OF FIGURES

PART ONE: THEORY BACKGROUND

1.1 Rayleigh Scattering

Rayleigh scattering was first reported by British physicist, Lord Rayleigh (John William Strutt), as the elastic scattering of light by particles due to the polarizability of atoms/molecules that act as oscillating dipoles.[1] It is elastic polarization (i.e., the emitted photon is equal in energy to that of the incident one) because the molecule returns to the same ground state. An everyday illustration of Rayleigh scattering is the observation of a blue sky. When light is scattered off the molecules, which have diameters much smaller than the wavelength of light, the blue wavelengths are scattered more efficiently than red wavelengths because of their lower energy. Therefore, unless we look directly at the sun, we are observing radiation enriched in the more strongly scattered blue frequencies.

1.2 Raman Scattering

Raman Scattering (RS) was first reported in India in 1928 by Chandraskhara Venkata Raman and K. S. Krishnan.[2-5] Sir C. V. Raman performed his experiment with his apparatus that consisted of two parts: one, a lens that was used to focus sunlight onto the neat liquid sample; and two, a telescope that was used to detect the scattered light produced from the sample.[6,7] Raman's application of the physical concepts on molecular scattering and light diffraction were formally published in 1922 as "The Molecular Diffraction of Light." In that report, he presented his analyses on water and other liquids that he thought could allow him to prove a "feeble fluorescence." It became obvious to him that different liquids like organic vapors, and gaseous CO_2, N_2O, some crystals and amorphous solids had to be studied as well.

After the announcement of the Compton Effect in 1923 more publications of an

inelastic phenomenon intensified but none had presented an actual concept of it. A

pursuit to publish a feasible explanation of this phenomena resulted in several reports by

R. W. Wood;[3] A. Smekal;[8] Kramers with Heisenberg;[9] and Schrödinger by 1925.[10]

Through 1927, Raman was still convinced that the effect he was observing was that of the

Compton scattering electrons.[11] Nonetheless, his continuous research that included the

spectral analysis on numerous liquids, by using a mercury arc lamp, became fundamental

to his hypotheses which allowed him to conclude by 1928[12] that, "any exciting spectral

line is always accompanied by weaker lines" as he represented them in equation 1.2.1:

$$\omega_{ex} \pm \omega_{vib} \qquad\qquad 1.2.1$$

Equation 1.2.1 was used by Raman to recognize an exchange of energy between

the incident photon and the internal excitations of the scattering medium.[13] In his view,

these excitations corresponded to the partial exchange of energy into atomic vibrations of

the molecules.

Incredibly, this new Raman scattering or inelastic scattering effect could have

been identified fifty years earlier. Lommel in 1878 cited it as a characteristic

fluorescence that depended on the frequency of the exciting radiation and the identity of

the sample.[14] G. Landsberg and L. I. Mandelshtam published it in the Russian literature

in 1918[15] as a theory on "combinatorial scattering" as a subtle structure splitting in

Rayleigh scattering. Lastly, a report by L. Brillouin in 1922[16] mentioned a frequency

shifts in scattered radiation through applications of quantum mechanics. Ultimately, it

was Raman's keen attitude and perseverance that guided him to identify "A New

Radiation" which led him to earn the Noble Prize in 1930.

<center>**PART TWO: TECHNIQUE ADVANCEMENTS**</center>

2.1 Light Scattering and the Raman Effect

Light is an electromagnetic wave that propagates through matter as an oscillating electrical dipole that can be absorbed, scattered, or transmitted.[2] Today, the inelastic scattering effect from Raman spectroscopy is used to identify the vibrational modes of a molecule.[17] This inelastic scattering or change of energy on the incident photon (hΔv) is equal to the energy gap between the ground and vibrational excited states of a molecule whose fundamental vibrational frequency is *v*.[13,15] Therefore, when light is scattered inelastically from the sample, the molecular vibrations may appear spectrally as side-bands in the scattered radiation, thus revealing the spectral fingerprint, which can be used to identify the changes around the molecular structure.

The interaction between radiation and the states of the molecule is studied in terms of change in energy (ΔE), frequency (v), or wavenumber ($\bar{v}$) scales and can be represented by equation 2.1.1:

$$\Delta E = hv = hc\Delta\bar{v} \qquad\qquad 2.1.1$$

Raman scattering is a feeble signal because only about ~1 photon (produced by about one among [1.0×10^8] scattered photons) interacts with the nuclear motions of the molecules,[18] by distorting (polarizing) the cloud of electrons that orbits the nuclei. As a result, the molecule is brought into a "virtual state" that is not stable and the photon is then re-radiated immediately leaving the molecule in an excited or de-excited state. The energy difference of the scattered versus the incident photon is equal to one vibrational quantum of the molecule.[19] It differs from resonant infrared absorption because it occurs with no corresponding upper state energy levels. It involves the formation of a complex

<center>14</center>

between the light and the molecule, which is followed by the scattered radiation, that is

emitted back essentially instantaneously (Figure 1) as expressed in equation 2.1.2.
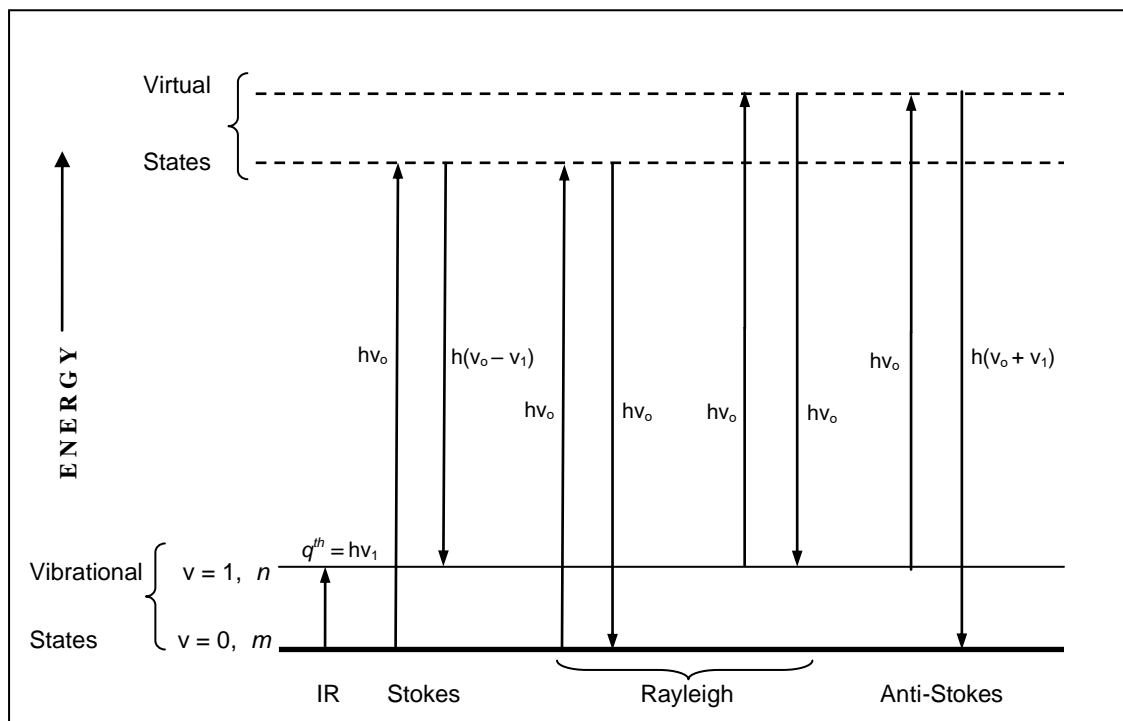
Figure 1. Energy level diagram of the Rayleigh and Raman scattering processes; Raman bands appear at $h(v_o - v_1)$ and $h(v_o + v_1)$.

Figure 1 represents a descriptive diagram for a diatomic molecule with level $v =$ 1, or where the fundamental exciting line of energy h_{v1} is above ground state.[2,4,6] The absorption of photons with frequency v_1 may be observed in the IR spectrum (representation for heteronuclear diatomic molecule).[5] When the radiation of energy h_{v0} is incident on the molecule, the bulk of the radiation is transmitted in a non-absorbing sample. A small fraction is re-radiated in all directions elastically (with no change in energy) which is called Rayleigh scattered light; an even smaller fraction of the radiation is the inelastically scattered Raman effect where two different events are possible: (1) molecules in ground state can give rise to the Stokes-Raman scattering with energies, $h(v_o$

– v_1), or (2) molecules in a vibrational excited state can scatter inelastically back to ground state giving an Anti-Stokes Raman scattering with energy $h(v_o + v_1)$.

In each of the elastic or inelastic processes the energy of the virtual state is defined by the energy of the incoming laser.[20] At room temperature, the number of molecules that populate the ground state level is much larger, thus the majority of the RSs are reported as Stokes-Raman. In turn, the ratio of the intensities between Stokes and Anti-Stokes scattering depends on the molecules that exist between ground and excited vibrational levels represented by the Boltzman Equation seen in equation 2.1.2:

$$(N_n/N_m) = (g_n/g_m) \cdot e^{[(E_n - E_m)/(kT)]} \qquad 2.1.2$$

where N_n is the number of molecules in the excited vibrational energy level (n),

N_m is the number of molecules in the ground vibrational energy level (m),

g_n is the degeneracy of the level n,

g_m is the degeneracy of the level m,

$E_m – E_n$ is the difference in energy between the vibrational energy levels,

k is the Boltzman's constant, and

T is the temperature in degrees Kelvin.

The degeneracy of the vibration is represented by g above and since some vibrations can occur in more than one way, g represents the number of components that cannot be identified independently. For most states g is equal to 1 with possible values of 2 or 3 for vibrations with different symmetry.

2.2 Vibrational and Rotational States of a System

The vibrational excitation of a molecule can be visualized with a Morse curve (Figure 2).[20,21,22] A transition between the ground state ($v = 0$) and the first excited state

($v = 1$) represents the absorption of one quantum of energy. On each vibration, the relationship between frequency, the mass of the atoms, and the bond strength of a diatomic molecule expressed by the Hooke's Law in equation 2.2.1:

$$v_{vib} = (2\pi c)^{-1} \cdot (K/\mu)^{1/2} \qquad\qquad 2.2.1$$

where c is the velocity of light,

K is the force constant of the bond between atoms/molecules A and B, and

μ is the reduced masses of atoms/molecules M_A and M_B identified in equation 2.2.2:

$$\mu = (M_A M_B) \cdot (M_A + M_B)^{-1} \qquad\qquad 2.2.2$$

The Morse potential energy is plotted along the y-axis and the inter-nuclear separation is along the x-axis seen in Figure 2. Each horizontal line depicts a vibrational state within the electronic state of a molecule. The first few energy states are approximately parabolic where the Hooke's law approximation applies.[21,22] When the harmonic oscillator is solved using the Schrödinger equation, the energy levels are found as a function of the quantum number v represented in equations, 2.2.3 and 2.2.4:

$$E_v = h v_{vib} (v \pm \tfrac{1}{2}) \qquad\qquad 2.2.3$$

$$\Delta v = \pm 1 \qquad\qquad 2.2.4$$

This means that with this simple model, vibrational energy quanta are absorbed in increments of $\Delta E = (h/2\pi c) \cdot (K/\mu)^{1/2}$. Thus, an application of this formula would correctly discerns the vibrations from the chemical bonds, between the carbon and hydrogen (C-H) and carbon and iodine (C-I) by showing a 3000 cm^{-1} mark that is produced by the former and a 500 cm^{-1} mark produced from the latter.
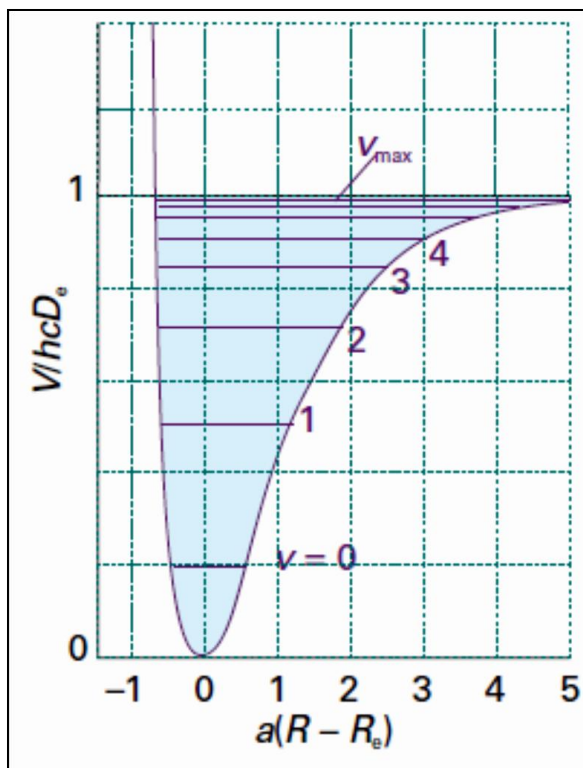
Figure 2. The Morse potential energy curve depicts electronic state of a diatomic molecule.

2.3 Origin of the Stokes Raman Scattering Modes

Polarization of a molecule can be induced by the oscillating dipole of an electromagnetic wave. It results in the effective spatial separation of opposite charges around a spherical molecule[23] that progress into a dipole moment caused by the incident electric field $\mathbf{E}$ (variables represented in bold differ with respect to those in initial formulas). Mainly, the induced dipole moment is composed by the distortion of the electrons that are spread around the surface expressed in equation 2.3.1:

$$\boldsymbol{\mu}_i^{ind} = \alpha\mathbf{E} \qquad\qquad 2.3.1$$

In this equation, $\mathbf{E}$ changes with time, and therefore the induced dipole moment, $\boldsymbol{\mu}_i^{ind}$ is also time-dependent, according to the electric field of the incident light, as seen in

equation 2.3.2:

$$E = E_0 \sin 2\pi v_i t \qquad\qquad 2.3.2$$

where $\mathbf{E_0}$ is the electric field at time $t = 0$ and

v_i is the frequency of the incident light.

The two vectors quantities, the induced dipole $\boldsymbol{\mu_i}^{\mathbf{ind}}$ and the inducing electric field $\mathbf{E}$ are graphically represented in Figure 3.[24-26] This selection rule is represented as the resulting data from the plot of the normal mode (or y-axis, Figure 3) versus the displacement, Q (or x-axis, Figure 3)[3,24] which applies to the change in polarizability. In fewer modes of vibration the differential, $\partial\alpha/\partial Q_q$ represents the radiation changes with respect to the displacement changes from the centre of mass of the molecule. This partial differential is used to determine either: (1) Raman activity, if it is roughly antisymmetric with respect to Q, or (2) to Raman inactivity, if it is nearly symmetric with respect to Q. In conventional (non-resonant) Raman scattering, the symmetry of the tensor is $\alpha_{ij} = \alpha_{ji}$ is plotted in terms of α that represents the radiation out of the molecular centre of mass which depicts a three-dimensional surface.

The reciprocal of the square root of the polarizability is graphed this way and its resulting surface is known as a polarizability ellipsoid. Any change in size, shape, or orientation of such polarized ellipsoid during a normal vibration, will make it a Raman active mode.[25] Next, the polarizability $\boldsymbol{\alpha}$ changes linearly with the vibrational amplitude of the molecule for small amplitudes.[23,25,26]
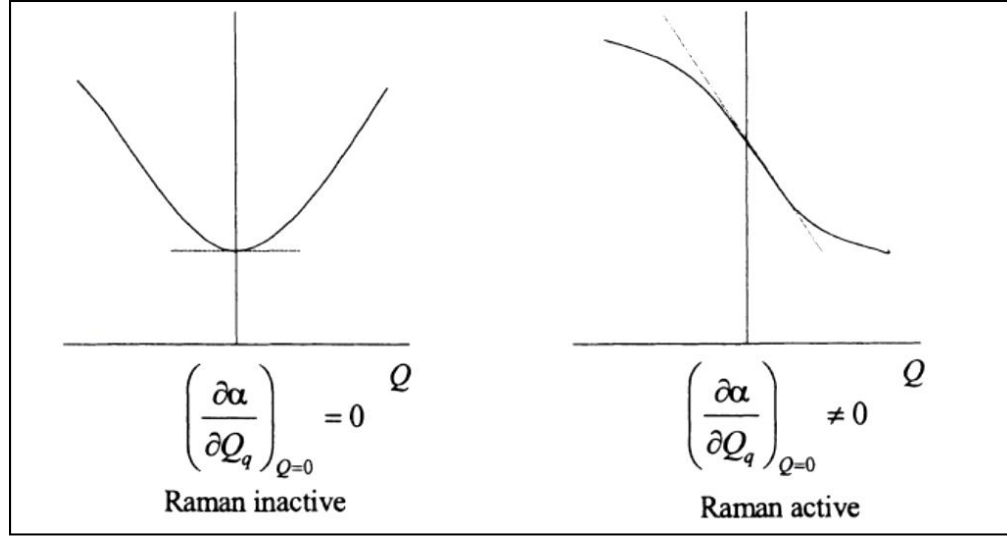
Figure 3. Representation of the Raman selection rule for a change of polarizability with the normal mode ($\frac{\partial \alpha}{\partial Q}$, y-axis) versus the displacement along the normal mode (Q).

The 'q^{th}' or vibrational normal mode of the molecule is represented by $\mathbf{Q}_q$, where the change in $\boldsymbol{\alpha}$ can be expressed with respect to time according to equation 2.3.3:

$$\alpha = \alpha_0 + \sum_q \left(\frac{d\alpha}{dQ_q}\right)_{Q=0} \cdot \mathbf{Q}_q \qquad 2.3.3$$

where $\boldsymbol{\alpha_0}$ is the polarizability evaluated at the equilibrium configuration from which the vibrational normal mode can be expressed using equation 2.3.4:

$$\mathbf{Q} = \mathbf{Q_0} \sin 2\pi v_q \mathrm{t} \qquad 2.3.4$$

where v_q is the corresponding natural frequency of the molecular vibration by substitution of equation 2.3.4 into equation 2.3.3, the total change of $\boldsymbol{\alpha}$ is shown in equation 2.3.5:

$$\alpha = \alpha_0 + \sum_q \left(\frac{d\alpha}{dQ_q}\right)_{Q=0} \cdot \mathbf{Q_0} \sin 2\pi v_q t \qquad 2.3.5$$

where μ_i^{ind} is the time-dependent that is solved after the fluctuations represented by equations, 2.3.2 and 2.3.5 which are then substituted into equation 2.3.1 with the use of the trigonometric identity, $\sin \alpha \sin \beta = \frac{1}{2} [\cos (\alpha - \beta) - \cos (\alpha + \beta)]$ for the result

expressed in equation 2.3.6:

$$\mu_i^{ind} = \left[\alpha_0 + \Sigma_q \left(\frac{\partial\alpha}{\partial Q_d}\right)_{Q=0} \cdot Q_0 \, sin \, 2\tau v_q t\right] \cdot E_0 \, sin \, 2\pi v_i t =$$

$$= \alpha_0 \cdot E_0 \, sin \, 2\pi v_i t + \Sigma_q \left(\frac{\partial\alpha}{d\partial}\right)_{Q=0} \cdot Q_0 \cdot E_0 \, sin \, 2\pi \, v_q t \, sin \, 2\pi v_i t =$$

$$\mu_i^{ind} = \alpha_0 \cdot E_0 \, sin \, 2\pi v_i t + \Sigma_q \left(\frac{\partial\alpha}{\partial Q_q}\right)_{Q=0} \cdot Q_0 \cdot E_0 \left[cos \, 2\pi\left(v_i - v_q\right)t - cos \, 2\pi\left(v_i + v_q\right)t\right] \quad 2.3.6$$

Equation 2.3.6 represents the scattered radiation that arises from the fluctuating dipoles of the molecule.[27]   The time dependence of the polarization for a vibrating molecule is expressed within the radiation field by three distinct terms: 1st term, is $\alpha_o \cdot E_0$ sin $2\pi v_i$ t which is the Rayleigh scattering or dominant effect (produced by about one among $[1.0\text{x}10^3]$ scattered photons); the 2nd and 3rd terms are $cos 2\pi(v_i - v_q)t$ and $cos 2\pi(v_i + v_q)t$ respectively, represent a feeble scattering event from the Raman effect (produced by about one among $[1.0\text{x}10^8]$ scattered photons). Both of these effects involve a change in the frequency of the emitted light that results from a transfer of energy between the molecule and the radiation field as it was hypothesized by Sir Raman.

Moreover, the Raman effect is composed in itself by two subtle, but very distinct events: first, by the anti-Stokes scattering event that is represented by the second term, $cos \, 2\pi(v_i + v_q)t$ (equation 4.6) which it is caused by the transfer of energy to the molecule, from the radiation source and the augmented frequency from the scattered light; and second, by the Stokes scattering event that is represented by the first term, cos $2\pi(v_i - v_q)t$ (equation 4.6) which it is caused by a transfer of energy from the field of radiation to the molecule and the reduction in the frequency of scattered light (Figure 1).[27]

According to classical theory, a Raman scattering is observed by the application

of equation 2.3.6 (Figure 3) which follows the condition set in equation 2.3.7:

$$\left(\frac{\partial \alpha}{\partial Q_q}\right)_{Q=0} \neq 0 \qquad\qquad 2.3.7$$

This expression provides the selection for conventional Raman scattering, where

only modes following this rule are Raman active and contribute to the Raman effect

(Figure 3).[23,24,27] However, this treatment cannot predict the frequency shifts of the

Raman effect precisely, nor the magnitude of its scattering. To determine such values

from the scattering cross sections, a quantum mechanical treatment of the cross section is

required (not addressed here). Also, an introduction of the Cartesian co-ordinates is used

to express the dipole moment (in equation 2.3.1) along with a matrix representation of the

explicit form of the second-rank polarizability tensor, $\boldsymbol{\alpha}$ (not addressed here).

2.4 Infrared (IR) Absorption and Raman Scattering

Analysis of the change in energy state of a photon under the influence of an

electromagnetic field would differentiate its change in energy state. An infrared (IR)

absorption occurs by a photon with an energy difference that extends from state m to

state n[29,30] (small arrow, bottom left in Figure 1). IR absorption requires a change in the

dipole moment as the molecule's vibrational motion modifies the dipole of the molecule.

If there is any loss in beam power during an IR spectroscopy reading, it would occur at

the specific frequency used to analyze the sample. This is the case when a given

vibrational mode (i.e., the frequency at which IR absorptions would appear) is observed

with the same frequency shifts for a Raman scattering.[28]

During IR absorptions the IR photon is annihilated by the molecule and the

molecule's vibrational energy is then increased by that photon's energy. This process

matches the frequency of vibrational resonance,[6] when the most intense IR absorptions

are caused by the most asymmetric vibrations that result in the largest changes in the dipole moment of the molecule.

Predicting Raman activity in a molecule is not as simple as determining its IR activity.[27,28] Assignments of the given vibrational mode to IR absorption and Raman scattering are completely different in nature.[29] Observed Raman scattering demands a change in polarizability of a second-rank tensor.[24] The change in polarizability or induced dipole moment of the molecule is a two-photon event that does not require matching of the incident radiation to the energy difference between the ground and excited states.[6] Since a single frequency is used in the irradiation of the sample, any radiation that scatters from the molecule is equal to one vibrational unit of energy, away from that of the incident beam and the detected frequency.

While a shift in frequency by the gained or lost vibrational energy of the molecule indicates Raman scattering; any scattered light that occurs at the frequency of the incident radiation characterizes Rayleigh scattering. Raman scattering (also Raman spectroscopy) occurs at a much higher energy radiation (in this study the ultraviolet, visible, and near IR or NIR ranges on the spectrum were reached). Raman scattering is relative to resonant IR absorption because it measures the difference in energy in the scattered photon between the vibrational states of n and m. This total energy in RS is represented by the Stokes and anti-Stokes vertical arrows indicated in Figure 1. Therefore, in both IR and RS patterns, a basic selection rule is followed where not all vibrations of a molecule can be produced by either one or in some cases, all can be both IR and Raman active. These techniques may be differentiated from one another because they usually reflect different intensity patterns. More often than not, the two processes complement one another.

2.5 Raman Scattering and Excited State Fluorescence

After the discovery of Raman scattering, its application to fluorescent compounds was usually avoided.[20,21] Not only can the Raman signal be obscured by a large fluorescence signal, but a photodecomposition process of the sample can be produced by the heat from light absorption too. Nonetheless, sometimes it is possible to record Raman scattering in the presence of fluorescence. Reports of a Raman scattering that was isolated from strong fluorescence showed that the Raman intensity went up by a factor of 10^6.[20] Such results were possible with the use of a laser beam that contained a frequency close to the frequency of an electronic transition of the sample.

Also, other reports about direct modifications used to overcome this effect can be summarized in three probable situations: (1) the presence of minor impurities could still be a cause of interference fluorescence, therefore the use of chemical or physical methods to purify the sample may obviate this inconvenience, (2) sometimes a continuous irradiation of the sample, by the laser beam, may burn off the impurities and thereby any fluorescence too, but this method can only be applied to robust samples, and (3) the difference in lifetimes between the nearly instantaneous Raman process, and from the real excited electronic state of fluorescence, may be exploited by using nanosecond or faster lasers.[26,29,31] Although, the total avoidance of fluorescence can also be achieved by using a longer wavelength of excitation and this is most often achieved with a reliable and stable NIR that is used in this report as a source for RS. A recent publication about the blockage of the auto-fluorescence (AF) background around extremely weak tissue Raman signals was achieved with the use of confocal Raman spectroscopy.[32]

Similarly, a considerable amount of study has been dedicated to Fourier

Transform (FT) Raman spectroscopy.[31,32] In FT-Raman, typically a NIR laser (usually Nd-YAG, 1064 nm) is used as a source and an interferometer to spectrally analyze the scattering. While it is exceptional for high resolution FT-Raman work, it has remained mainly in niche markets.

2.6 Near Infrared (NIR) and Raman Scattering

One important advance is having the ability to choose a laser wavelength suitable for the sample.[6,33] The combination of a NIR diode laser source and a multiwavelength integrating detector, or charge coupled device (CCD), can dramatically improve the signal to noise ratio of a Raman instrument. Also, the advent of the holographic notch filter used in the removal of Rayleigh radiation has profoundly improved Raman detection.

In the present report, the laser of a wavelength $\lambda = 785$ nm is just in the NIR range, and along a CCD detector and a holographic notch filter were used here. Noteworthy, the Raman scattering is its very strong dependence on frequency, where the probability of Raman scattering varies as ν^4.[6] Thus, scattering intensity is related to the fourth power of frequency where intensity increases with decreasing wavelength. The selection of a laser with a specific wavelength of light depends on the type of excitation to be made, since it is imperative to avoid fluorescence in most cases. Examples of different operating wavelengths are shown in Figure 4. One tradeoff is that for shorter wavelengths, the sensitivity increases rapidly, but so does the propensity of the system to fluoresce and flood the system with unwanted light and attendant noise.
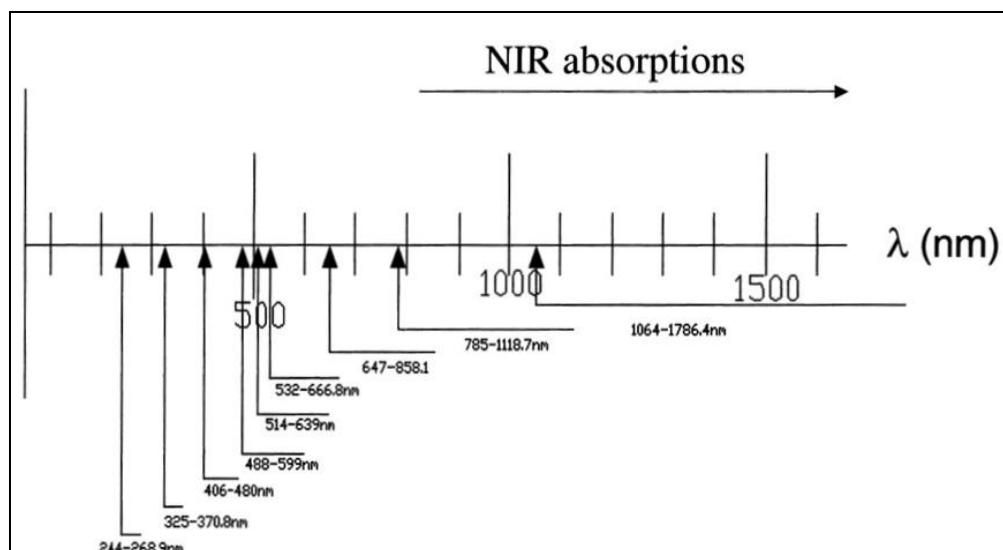
Figure 4. Typical laser excitation wavelengths and the corresponding Stokes Raman shift for 3800 cm^{-1}.

2.7 Localized Surface Plasmon Resonance (LSPR)

Light absorption and scattering process by a metal sphere is at the core of the LSPR theory.[34] LSPR effect can be understood in the following way: (1) the surface of a metal (e.g. silver) sphere is the surface of a fluid of bound electrons; (2) like any fluid, the electron density in the metal sphere can oscillate; (3) because the electrons are charged, they can under certain circumstances, coupled to the oscillating EM field of light; and (4) a resonant coupling interaction between light and this electronic fluid is referred to as a localized surface plasmon resonance or LSPR. In turn, this LSPR results in intense electric fields at the metal surface and these fields are much stronger than those of the incident light. The LSPR phenomenon can be described as a cloud of electrons that is driven by electromagnetic radiation, when it pushes them away from equilibrium state. Meanwhile, the heavier, positively charged nuclei that remain stationary exert a counteracting force acting to restore the electrons back to equilibrium position and thus, an oscillation of electrons is formed (illustrated in Figure 5). These interfacial fields are

the ones believed to underpin the enhancement in surface enhanced Raman spectroscopy.
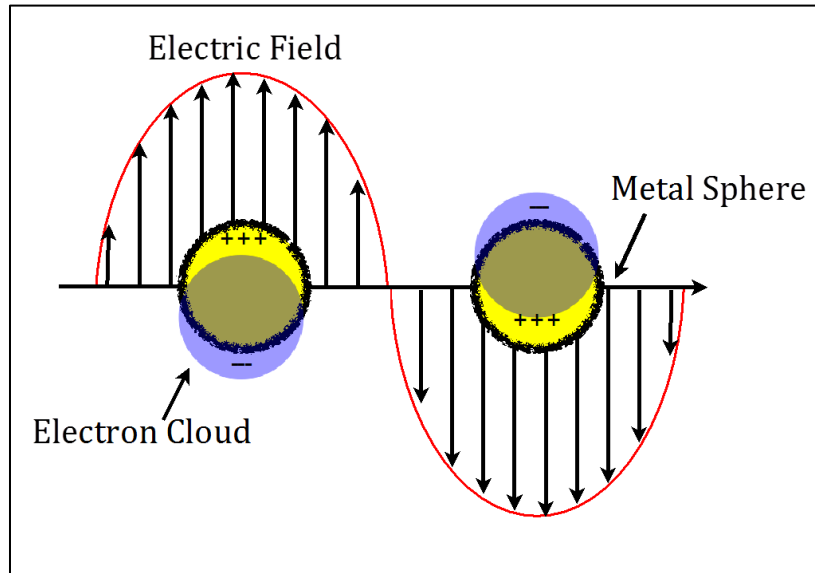
Figure 5: Surface Plasmon on metal surface shows polarization of the conduction band electrons in metal Nps that is induced by the incident electromagnetic radiation.

2.8 Surface Enhanced Raman Scattering (SERS)

The first surface-enhanced Raman scattering or SERS, event was described in 1973 by J. McQuillan as a "surprisingly strong and potential-dependent Raman signal from pyridine-adsorbed, from a solution onto a silver electrode roughened, by successive oxidation-reduction cycles…[and with] an enhancement by a factor of 10^6" (Figure 6).[35] Reports that followed from Jeanmaire and Van Duyne perceived SERS as a "…Raman signal enhancement in the pyridine-on-silver system and proposed enhancement mechanisms based on electromagnetic and chemical effects," respectively.[36,37] Albrecht and Creighton also reported that SERS intensity was caused by more than an increase in surface area.[38] Subsequent studies on SERS have shown that copper, silver, and gold are good SERS substrates.[37,38]

Twenty years hence, a resonant form of SERS is now believed to be responsible
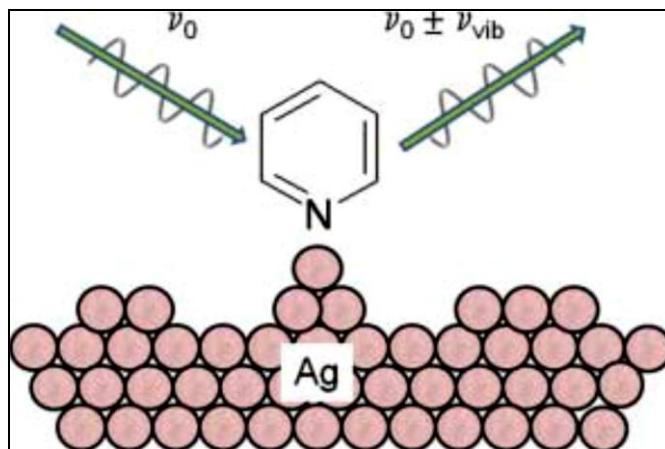
Figure 6. The SERS effect is represented through the adsorption of pyridine onto silver. Both the incident and scattered intensities are influenced by the enhanced field at the surface of silver that results from the localized surface plasmon excitations.

for single molecule detection (SMD) with an enhancement factor of up to ~10^{14}.[39]

Today, a combination of two or more techniques include monitoring the spectral SERS in UV-Vis light (presented in this study).

The use of nanoparticles across the fields of analytical chemistry, biochemistry, and physics has resulted in a surge of reports from the SERS phenomena. Some of these developments include: a single nanoparticle probe (SNP),[40] a two-analyte probe with a thickness functionalized via gold nanoparticle (Au-NP) coupling that was used in the SERS detection of residual pesticides, at the surface of fruit peels,[41,42,43] in drinking water,[44] and in the study of common biological fluids.[45] The high sensitivity of SERS probes also enabled the detection of low pM label concentrations from a light scattering immunoassay at a surface of polystyrene probes.[46] Another report of size-tunable Ag shells in an Au@Ag core-shell structure produced optimal and highly sensitive SERS efficiency.[47] Other tests have found that new roughened surfaces, aggregated colloidal suspensions, electrodes, cold substrates, and metal-island films and colloids, silver island films and silver coated beads were appropriate for LSPR enhancement of SERS.[48,49-52]

PART THREE: THEORY ON SURFACE ANALYSIS

3.1 Mie Theory and the Raman Scattering Cross Section of Gold NPs

The applied study of small spherical metal optical properties (reported here as Au@Ag NPs) was first presented in 1908, by German physicist Gustav Mie.[53] Mie developed his theory in the form of a set of equations. He described the scattering and absorption of light by a small (absorbing) sphere. His approach made reference to the color phenomena and polarization effects in the metals colloids of Au, Pt, Ag, Cu, Ni, and Co. A similar approach was attempted by Ehrenhaft, with a claim that for a limiting case of the particle size approaching zero, a maximum scattering would occur at an angle of 120° when in fact fifty, Mie had correctly hypothesized fifty years earlier that it would be at 90°. One of Mie's theoretical calculations expressed the spatial electric field values when a plane electromagnetic wave hits a spherical particle. The particle in question was of a certain refractive index and it was embedded in a medium, m_0. In this setting, as in many others, the Mie equations totally fulfill and continue with the Maxwell equations. The Mie equations utilize spherical coordinates (r, θ, ϕ) and the dimensionless size parameters of x = 2πrm/λ and α = 2πrm$_0$/λ with the assumption that the particle radius 'r,' is much smaller than the light wavelength (r << λ) which avoids the possibility of an electrical multipole thus, the electric field may be taken as a constant. As a result, Mie was able to predict the extinction cross section for a spherical nanoparticle dipole, a result that was still applicable to this study as it is stated in equation 3.1.1:

$$\sigma = \frac{9\,V\,\varepsilon_m^{1.5}}{c} \cdot \frac{\omega \cdot \varepsilon''(\omega)}{(\varepsilon(\omega)' + 2 \cdot \varepsilon_m)^2 + \varepsilon''(\omega)^2} \qquad 3.1.1$$

where σ is the scattering cross section,

$V = \frac{4}{3}\pi r^3$ is the particle volume,

c is the speed of light,

ε_m is the dielectric of the environment,

ω is the angular frequency of light, and

$\varepsilon = \varepsilon(\omega)' + i\varepsilon(\omega)''$ is the complex dielectric of the metal.

Equation 3.1.1 shows that the extinction cross section depends on two factors: (1) the dielectric field of the environment and (2) on the volume of the (nano) particle.[51] This is referred to as the long-wavelength approximation of the dipolar resonance. By applying this formula, Mie assumed that the plasmon resonance had to be centered on a light frequency composed by a real part, of a complex dielectric, with twice the magnitude of the dielectric constant of the medium, i.e. $\varepsilon(\omega)' = -2\varepsilon_m$.[53,54] This equation also explains the different colors associated with the different sizes of the NPs. Other studies have also exploited this phenomenon through the creation of colorimetric sensors sensitive to the surroundings of the particles, and most dramatically to the aggregation of NPs.[55-58] The peak visible near 520 nm is attributable to the dipolar LSPR band of Au@Ag NPs (introduced in Figure 13 below).

3.2 Enhancement Factor from SERS of Aggregated Au@Ag | R6G

The absolute cross section exhibited by individual molecules in SERS settings can be estimated as is the case with rhodamine 6G (R6G) on nanoparticle aggregates in the Au@Ag system.[50,51] For this purpose, the following knowledge is required: (1) the unenhanced Raman cross section at the laser wavelength; (2) the integral, unenhanced Raman signal taken of the analyte using the instrument in question; (3) knowledge of the concentration of the analyte molecule in the enhanced setting; and (4) The integral signal of the SERS active molecule. The relative enhancement factor (EF) can be defined with

the application of Equation 3.2.1:[61-71]

$$EF = \frac{I_{SERS}/N_{Surf}}{I_{Raman}/N_{Vol}}$$

3.2.1

$$\sigma_{SERS} = \sigma_{Raman} \cdot EF$$

where I_{SERS} represents the intensity of the SERS signal,

N_{Surf} is the number of molecules adsorbed to the nanoparticles in the sample,

I_{Raman} is the normal Raman intensity,

N_{Vol} is a given number of molecules in the excitation volume, and

σ is the absolute cross section that derivates from the indicated process.

Most molecules adsorbed to Au@Ag NP aggregates exhibit intense SERS when

irradiated at 785 nm.[72,73] This is likely due to the fact that an intense LSPR band that is

unique to Au@Ag particle aggregates is formed between 770 and 860 nm. In general,

there are numerous LSPR modes observed from the large variety of nanoparticles, and all

vary in compositions, shapes, and sizes.[74-76] The nanoscopic gaps in between aggregated

nanoparticles presumably give rise to the most intense SERS signals.[76] These gaps are

known as "hot-spots" and can exist between two aggregated particles. An interparticle

gap between these nanoparticles (~1 nm) was identified as the most likely place where

target molecules could get attached.[77,78] The intense SERS spectra are generally assigned

to the junction of nanoparticle dimers and trimers which had been reported to be

frequently larger than single dipolar particles[75,79,80] More explicity, dimerization of two

nanoparticle of Au@Ag, is a predominant form of aggregation that offers an optimal

SERS signal correlated by LSPR. This LSPR-SERS connection is not quite definitive

however.

Optimal SERS enhancements were also reported in the form of 'hot spot'

emitters, at 785 and 830 nm wavelengths and appeared much longer than the ones associated with the LSPR peaks.[77] These results suggested that a mechanism other than far-field observable LSPR could be involved in the creation of the observed hot spots associated with NP-aggregates.[50] Nonetheless, the intense SERS and the consistent correlation with aggregation is the principal motivation for the current study.

3.3 Theory on the Origin of the SERS Mechanism

The mechanisms of the SERS effect are broadly classified as either electromagnetic (EM) or chemical enhancements (CE).[73,81,82] In the CE mechanism, a charge-transfer occurs when the analyte is adsorbed onto, or is held in close proximity to the metal surface.[74,76,83] Also, in a CE mechanism a chemical bond between the adsorbate and the surface is created, at the point where a signal excitation occurs through a transfer of electrons, from the metal to the molecule and back to the metal again. The contributions from CE include chemical bonding, electron transfer, resonance with electronic states along with a strengthening of an inhomogeneity of local fields with respect to isotropic radiation.[48,84-87]

The EM enhancement involves a linear interaction between the analyte and the electric field of the plasmon. The EM mechanism occurs at a significant depth from the surface of the metal –i.e., from a second, third, and subsequent molecular layers where enhancements were reported to reach a depth of 20 Å–. The CE mechanism is only possible from the first layer of the analyte to the surface. When the two electric fields, the incident ($\mathbf{E_I}$) and the re-radiating one ($\mathbf{E_R}$) encounter similar plasmon resonances the electric field enhancement in the RS scales up to $|\mathbf{E_I}|^2 \cdot |\mathbf{E_R}|^2$.[69,87-54] According to theoretical frameworks, these plasmonic optical fields have been augmented by factors of

$(100^2)(100^2)=10^8$ fold of total enhancement.[49,54] The operative LSPR mode of the nanoparticle makes this possible since both, the incident $\mathbf{E_I}$, and the Raman shifted $\mathbf{E_R}$ occur at near-enough resonance. Thus, the overall enhancement depends on the magnitude of the incident electric field $\boldsymbol{E}(\boldsymbol{\omega})$ raised to the fourth power that is expressed in equation 3.3.1:

$$EF_{EM} \propto |E(\omega)|^2 \cdot |E(\omega')|^2 \approx |E(\omega)|^4 \qquad\qquad 3.3.1$$

where $E(\omega)$ is the frequency dependent electric field at $\boldsymbol{\omega}$ the incident frequency, and $E(\omega')$ is the frequency dependent electric field at the Stokes shift frequency $\boldsymbol{\omega'}$.

Therefore, for small Stokes shift values the equation 3.3.1 applies a value that corresponds to $EF_{EM} \propto |E(\omega)|^4$.[54] The maximum EF_{EM} is normally found slightly blue-shifted from the plasmon resonance the peak in $\mathbf{E(\omega)}$. Hence, the aggregated system is ideal for the detection of diffusing molecules for Au@Ag (which is detectable via extinction measurements) since the aggregate LSPR appears around 775 and 800 nm (Figure 7).

3.4 DLVO Theory of Colloid Interaction of Aggregated Au@Ag NPs

By 1941, the theoretical calculation of the interaction of colloid particles was ratified by Derjaguin, B., Landau, L., Verwey, E. and Overbeek, J. or DLVO theory.[88] DLVO explains quantitatively the aggregation of aqueous dispersions as a combination of the van der Waals (vdW) forces of attraction, V_{att} (kT) and the forces of repulsion, V_{rep} (kT) that are due to the interactions of the electrical charges of the colloidal NPs. More specifically, the DLVO theory accounts for the full electrical double-layer and therefore for the screening of like charges by electrolyte ions. Thus, DLVO can be applied to account for the aggregation of NP suspensions as salt is being added.[89]
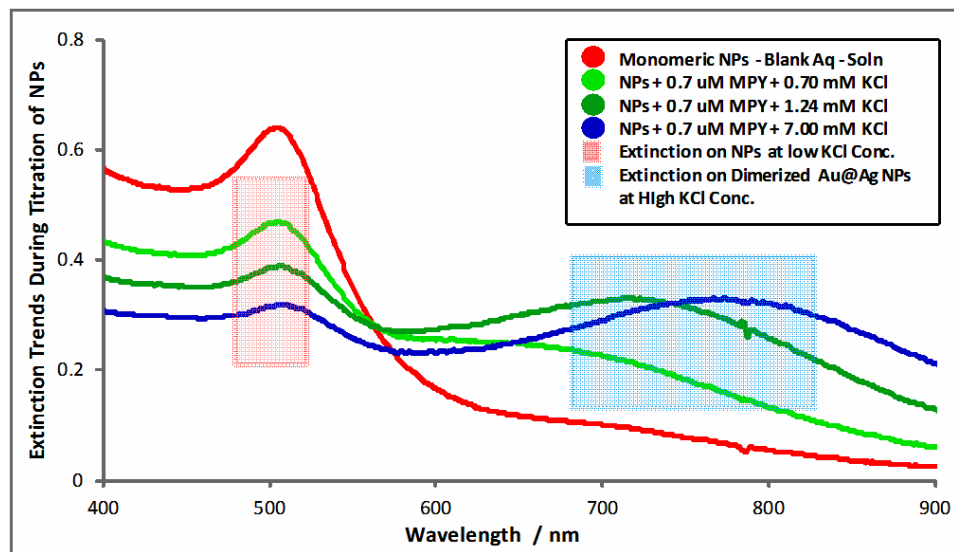
Figure 7. Extinction peak at λ≈515 nm of an Au@Ag NP solution, red box area is at 0.70 μM MPY and blue box area is at NIR spectra aggregated NPs.

These interacting forces are known as Stern Layers and are illustrated in Figure 8. The balancing of microscopic electrical forces in colloidal particles starts by one molecule from the first colloid, which has a vdW attraction to each molecule from the second colloid and vice versa.[90] The DLVO theory provides a framework that explains the phenomenon of NP aggregation and at the same time, may be used to determine the SERS phenomena.[50,51] It explains the interaction between small and large size particles, as a deposition process, to a large diameter molecule or a planar substrate. This net energy can be plotted point by point, at each distance, where a curve is drawn by the difference between the small and the larger energy values.[89]
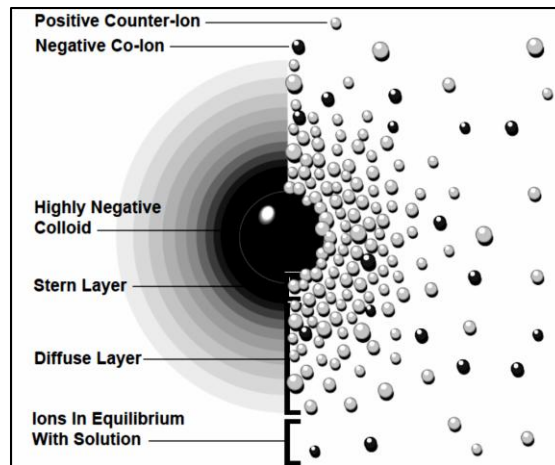
Figure 8. Microscopic electrical forces across the double Stern layer of the ionic conditions that surround a charged colloid particle.

Figure 9 shows the function of the interparticle distance from the sum of all of the attractions and repulsions that equals to the total force experienced by nanoparticles.

Predispositions of colloidal particles to cluster, or to stay apart, are explained by the DLVO theory by either of two identical particles (during a homoaggregation) of two different particles (during a heteroaggreation).[89,91,92] This process is initiated when the counter-ions (positive ions) are attracted by the presence of the negative colloid charges. In this case, a strongly charged layer around the surface of the colloid within the Stern layer starts to form.[89]

The point of maximum repulsive energy and the stability of the system are indicated by the height of the barrier.[50,89] When two molecules are on a collision course they must have enough kinetic energy to "jump over" this energy barrier. As soon as the barrier is passed the resulting net interaction is attractive and the particles aggregate.

DLVO theory treats colloid stability in terms of both attractive (vdW) and repulsive (electrostatic) forces.[51,93] Hence, DLVO provides a framework for understanding the phenomenon of nanoparticle aggregation which is a crucial
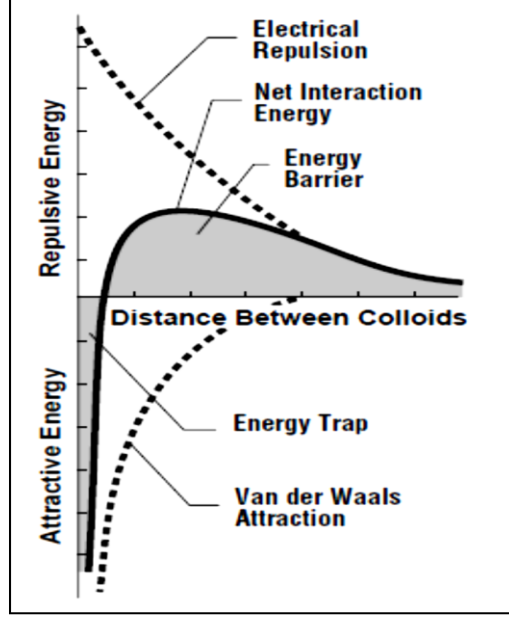
Figure 9. Electrostatic repulsion curve has a maximum value when they are almost touching and decreases to zero outside the double layer.

determinant of SERS phenomena in Au@Ag systems. This maximum energy is related

to the surface potential and the zeta potential. On the other hand, the negative curve that

represents the vdW attraction is the real value of forces on individual molecules.[89]

3.5 Estimates of the ζ -potential as a Function of R6G Adsorption to Au@Ag

The first term in the DLVO barrier calculation is the electrostatic repulsive energy

for the two spheres of radius a with zeta potential (ζ) which approach each other in a

medium of Debye length κ^{-1}, with r as center to center distance as seen in equation 3.5.1:

$$V_{rep}(k_B T) = 4\pi\varepsilon_r\varepsilon_o \left(\zeta \frac{a^2}{r} \right)^{\left[-\kappa a \left(\frac{r}{a} - 2 \right) \right]} \qquad 3.5.1$$

where ζ is the zetta potential around each molecule,

ε_r is the relative permittivity of water, and

ε_o is the vacuum permittivity with κ which is expressed in equation 3.5.2:

$$\kappa^2 = (2n^\infty e^2 z^2) \cdot (\varepsilon_r\varepsilon_o kT)^{-1} \qquad 3.5.2$$

where z is the valancy of the ions comprising the double layer (±1 in the present study),

e is the electronic charge, and

n^∞ is the number density of ion in bulk solution which was estimated in solution

conductivity by using equation 3.5.3:[94]

$$\sigma = \Lambda cz \qquad\qquad 3.5.3$$

where σ is the specific conductivity of the particle solution,

Λ is the equivalent conductivity of the electrolyte solute (KCl in this report),

c is the electrolyte concentration and within the bounds of this estimate, and

$c = \mu$, is also the solution ionic strength.

From the calculation of μ, all conductivity is attributed to KCl which admittedly

neglects differences in the value Λ, between KCl and other less abundant constituents

such as hydrogen ion, nitrate, citrate and ascorbate.[51] However, given that a pH of 3.55

and the negligible calculated concentrations of other ions, this estimate is expected to

have only a minor impact on the ζ potential calculation. Therefore, as only minor

approximations are needed and considering the observed constant pH and conductivity, in

the freshly prepared NP solutions, there is little reason to expect that the trend in the

magnitude of the DLVO energy barrier should derogate severely from the one predicted

here.

In order to estimate the changes in the ζ potential of Au@Ag nanoparticles as

they adsorb R6G, aside experiments were performed to measure their electrophoretic

mobilities.[51] In them, 50 mL injections of nanoparticles were pipetted into a quiescent

solution of citrate buffer (adjusted to the same pH and ionic strength as in the optical

measurements) in a commercial gel electrophoresis apparatus that contained only

aqueous buffer and no gel. The electrophoretic mobilities of the particles were measured

under a 64 V/cm electric field, by observing the drift of the center of the particle aliquots

using a video camera. The resulting mobilities were then used to calculate the

electrophoretic mobilities of the particle specimens and in turn, calculation of the ζ

potential of the particles was done by applying the Smoluchowski Equation, which

relates the zeta potential (ζ) with the electrophoretic mobility (μ_e) using equation 3.5.4:

$$\mu_e = (\varepsilon_r \varepsilon_o \zeta) \eta^{-1} \qquad\qquad 3.5.4$$

where $\mu_e = v/E$ is the ratio of drift velocity of the particle to the applied electric field and

η is the dynamic viscosity of the solvent (water).

The second term in the DLVO expression is the attractive van der Waals

interaction energy between particles of radius a is expressed in equation 3.5.5:

$$V_{att}\,(\,kT\,) = -\frac{A}{6}\left[\frac{2a^2}{r^2-4a^2} + \frac{2a^2}{r^2} + ln\left(1 - \frac{2a^2}{r^2}\right)\right] \qquad\qquad 3.5.5$$

where att represents attractive forces,

A is the Hamaker constant which further equates to $\pi^2 C \rho_1 \rho_2$,

C represents the concentration, and

ρ the number densities of the two spheres under study.

The interaction between the two particles can be expressed by combining the

above two terms in equations 3.5.1 and 3.5.5 and by substituted them into equation 3.5.6:

$$V_{tot}\,(\,kT\,) = V_{rep}\,(\,kT\,) + V_{att}\,(\,kT\,) \qquad\qquad 3.5.6$$

By using accepted values of A[93] using the plots of V_{tot} versus distance for a

variety of ζ values, a corresponding trend was observed among the different measured

[R6G]. For larger ζ values, a peak in the energy could be seen as the distance decreases

toward contact as it is seen in Figure 10.[51]
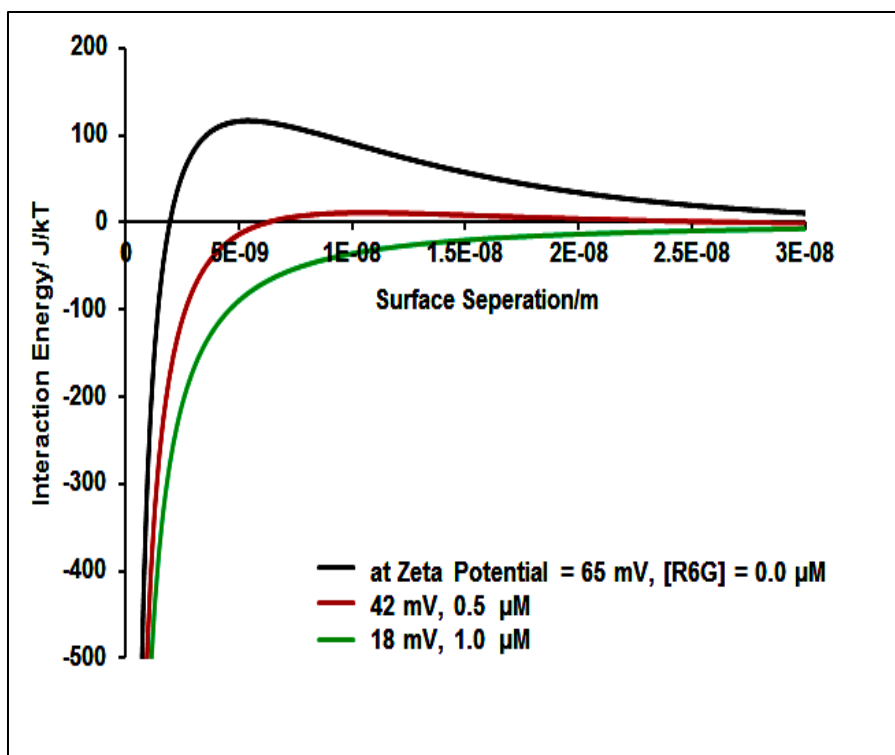
Figure 10. Theoretical potential energy relative to *kT* versus surface separations showing the plot for clean nanoparticles and pre-incubated NPs in 0.5 and 1 µM R6G where the trend towards aggregation clearly indicates aggregation for the 1 µM case.

This peak was responsible for the stability of the colloid solution and as ζ decreases, the peak disappears, and nanoparticle solutions were expected to aggregate. As expected, it was found that as ζ decreases the barrier started to disappear near $\zeta = 42$ mV (red band Figure 10). This result has significant relevance to this thesis because it allow us to conclude that the spectral changes are the result of aggregation which is a result that DLVO theory also supports.[51]

The integral SERS intensities, alongside aggregate extinction are plotted on the y-axes against the label concentration (either: R6G, MPY or MBA on the top, middle or bottom rows respectively) along the x-axes. In general, these plots show an onset, a peak, and a decay in the overall SERS signals which is closely tracked by the aggregate

39

extinction. The inset in the upper left corner in the graphs illustrating the DLVO

calculations derived from electrophoretic mobility measurements which enabled

estimates of the ζ- potential of the Au@Ag NPs. These results showed a decline in the

range that corresponded as a function of added R6G that occurred as an abrupt

aggregation during the micro-titration runs. For each [R6G] (Figure 11, top) the

approximate barrier to aggregation was computed using DLVO.[92] The observations of

the spectral signature of aggregation that appeared abruptly were produced at 1 μM

addition and were consistent with the above calculations that predicted the collapse of

Coulombic barrier at that point. Similarly, 4-mercaptopyridine (MPY) SERS and the

nanoparticle NIR LSPR coincide, but rise gradually and continue to rise over three orders

of magnitude in [MPY] (Figure 11, middle). In contrast, the 4-mercaptobenzoic acid

(MBA) SERS signals (Figure 11, bottom) are quite weak.

This trend was possible not because MBA does not adsorb to the monomeric

Au@Ag NPs (see below) but because MBA alone does not trigger aggregation as it

became evident, after the very slightly aggregate extinction signals that were generated

by the addition of KCl aggregant (~20 mM). The bottom panel in Figure 11 also includes

the wavelength corresponding to variation in λ_{MAX} for the localized surface plasmon

(blue, triangles). This scale bar indicates a red shift (up) of 1 nm. The upper left inset

shows the variation of computed DLVO barrier to particle aggregation as a function of

the estimated ζ-potential for three nanoparticle specimens incubated in [R6G]: 0.0, 0.5

and 1.0 μM.[51]
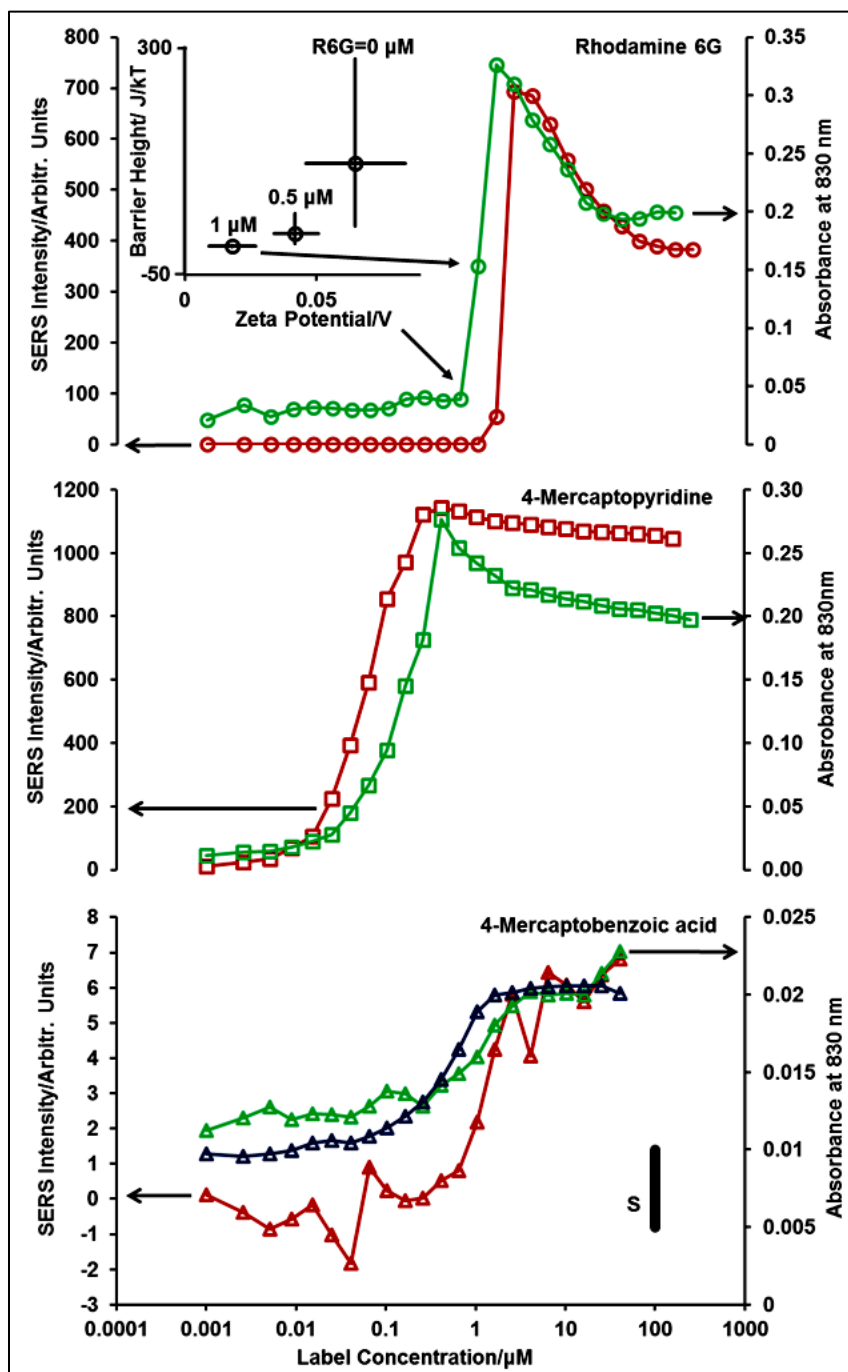
Figure 11. Variation of integrated Raman intensity (left scale, red symbols) alongside aggregate band extinction (right scale, green symbols) as a function of SERS label titrant concentration; R6G (circles, top), MPY (squares, middle) and MBA (triangles, bottom).

PART FOUR: EXPERIMENTAL METHODS

4.1 Synthesis of Gold Core Nanoparticles

The synthesis of gold cores was performed using the single-phase water based Turkevich method.[50,51,52] This synthesis involves a citrate reduction of Au^{3+} to Au^0 that causes nucleation of the Au metal, where more Au can crystallize onto and promote NP growth. The control of particle growth is determined by the amount of citrate solution added. Excess citrate partially passivates the incipient particle surface and the negative charge during growth does not allow particles to aggregate. The protocol for the core synthesis includes a 250 mL three-neck round-bottom-flask (cleaned four times with aqua-regia, a 4:1 mixture of concentrated HCl/HNO_3) that was adapted with 1-reflux-condenser and 1-Teflon coated stirring bar (under vigorous stirring) and atop of a heating mantle. All the reactions used fresh stock solutions prepared with ultrapure water (UPW, >14-16 MΩ Cm, recirculating Millipore polisher / deionizer / filter) and were delivered via filter-tipped (0.2 μm) syringe. The following are the steps used for this reaction: (1) addition of 95.0 mL of UPW; (2) addition of 300 μL of potassium tetrachloroaurate solution ($HAuCl_4$, Acros reagent grade, 0.10 M, 25.0 mL); (3) addition of 1.53 mL of trisodium citrate solution (Acros, 98%, 3.40 mM, 25.0 mL) under stirring at room temperature (r.t.) for 15 minutes; (4) allow the reflux to reach boiling point (x 60 minutes at 100 °C); (5) register when solution turns from a pale yellow into a ruby red; (6) cover the solution from light exposure and set aside until it cooled to near r.t. over a 30 minutes stirring.

4.2 Extinction Coefficient of Au Core Nanoparticles

At the end of the gold core synthesis an aliquot (~5 mL) was collected for benchmark measurements. Extinction measurements (silica cuvette, UPW blank) were made on a 1:1 mixture of gold cores plus UPW and once finished the core particles were stored at 4 °C.

4.3 Silver Shell Encapsulation of Au Core Nanoparticles

This thesis applies the synthesis encapsulation of gold core nanoparticles in a silver shell that was adapted from the chemical metal reduction procedure by Liu and Han.[42,50,51] In this procedure, the ascorbic acid reduces the Ag^+ into Ag^0 which will crystallize on the Au nanoparticles in the solution until it reaches a degree of coating.

This coating layer can be varied based on the amount of silver nitrate ($AgNO_3$) added to the solution (but it is known to have been performed at subsequent times). Since the Ag coats the Au nanoparticles that are already in solution, the concentration of nanoparticles is conserved from the Au nanoparticle synthesis. This stage was performed less than 24 h after our core synthesis had been completed. The following are the steps used in the process: (1) start a continuous stirring of 95.5 mL of Au cores, (2) addition of 14.2 mL of ascorbic acid (Fischer 99.8%, 1.00 mM); (3) dropwise addition 25.0 mL $AgNO_3$ (Acros, ultrapure grade, 1.00 mM) via a syringe pump (~40.0 μL / min); and (4) covering the apparatus with aluminum foil to avoid any unwanted reduction of silver metal by the action of white light.

4.4 Preparation of Stock Solutions

Solutions of R6G (Acros Organics), 4MPY (Sigma-Aldrich), 4-MBA (Sigma-

Aldrich) and KCl (Sigma, reagent plus $\geq$ 99.0%) were prepared from a 1.0 mM all the way to 0.001 mM from a 10 mM stock solution. According to the serial dilution in Table 1 each vial was labeled A, B, C, D or E.

Table 1. Serial diulution of a 10 mM stock solution used for solutions: A, B, C, D, and E.

4-MBA Label A	0.1 L	0.005 M	154.19 g.mol-1	0.077 g	1000 mg.g-1	77.095 mg
Label B	0.05 L	0.001 M	154.19 g.mol-1	0.0077 g	1000 mg.g-1	7.7095 mg

...

4.5 Instrumental Apparatus

Raman spectra were collected using an Enwave Optronics EZ-Raman (785 nm, 300 mW P_{MAX}) spectrometer, in a backscattering geometry and an optical resolution of ~7 cm^{-1} set to approximately 150 mW (or ½ P_{MAX}). Spectra were collected in an average of four, 4 s scans. Since the lens tube has a 7.00 mm focal length, the optical path of light was positioned at 5.0 mm inside the liquid volume (by accounting the thickness of wall in the cuvette of ~1 mm).[51] The cuvette was adapted with a small Teflon magnetic bar (ca. 600 RPM). A schematic of the table system is provided in Figure 12. Visible absorbance spectra were obtained concurrently to the Raman collection using an absorbance spectrometer, from Ocean Optics that is equipped with an LS1 tungsten halogen light source and coupled via a 400 μm multimode fiber optic cable to a pair of collimating lenses. Spectral acquiring was performed using an Ocean Optics USB 650 spectrometer.
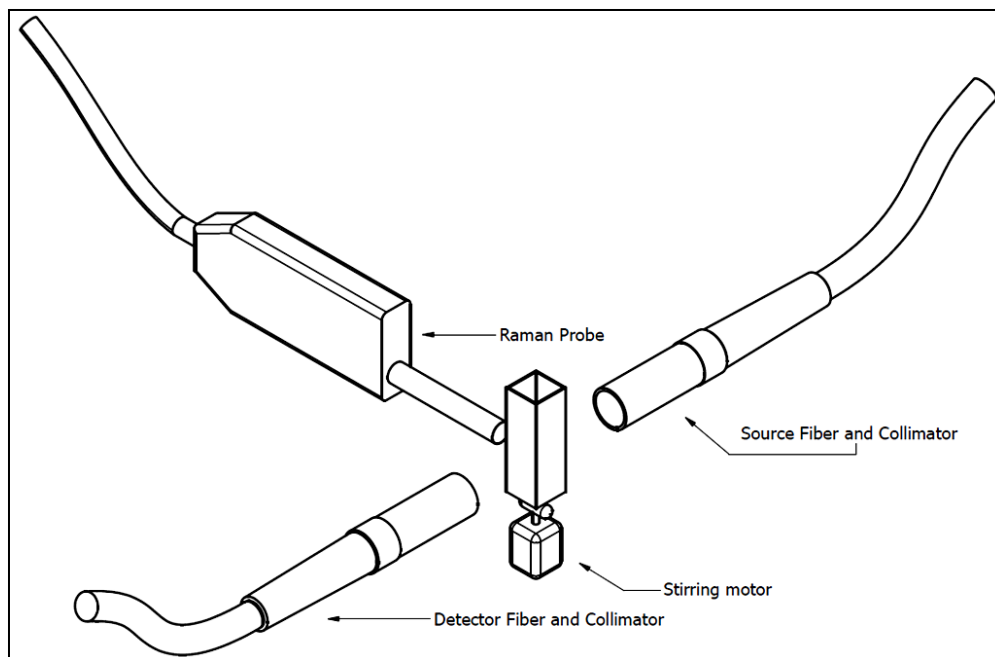
Figure 12.   Scheme of a fluorescence cuvette being interrogated by a backscattering Raman and a transmission visible extinction probe.at a coinciding foci in the NP-solution.

Data acquisition, storage and analysis were possible with the use of a National Instruments LabView 8.2 software routine.   The calculation of the Au@Ag surface potential also required the recording of the pH using a Beckman Φ43 pH meter, and temperature plus conductivity using a Cole-Palmer meter. In one case, the zetta (ζ) potential of NPs was obtained using a commercial gel electrophoresis apparatus from EmbiTec Run-One, and the potential transfer was recorded in a 5 minute video.

PART FIVE: SERS INTENSITY CORRELATION TO Au@Ag SYSTEMS

5.1 Experimental Objectives

To investigate and support any probable correlation between an enhanced SERS intensity and the aggregate extinction by LSPR in Au@Ag NPs within an aqueous solution setting of variable ionic strength.[43,50,51] Application of a SERS micro-titration where the titrant may either be a SERS label, or the KCl would be added gradually to a solution containing either the KCl or a SERS label and this would allow the observation of this phenomena. It is properly convenient that this setup could also record the SERS signals alongside the optical extinction spectra of the NPs.[54,55] Since aggregation is expected to be triggered by the SERS labels (R6G, MPY and MBA[56]) and the aggregant KCl, the role of each titrant during and after enhancement of SERS could be then analyzed. It is also expected that the intensity of the SERS response could appear to correlate to the aggregate absorption band measured at 830 nm.[42,50,51] The conditions for a sensitive SERS response are presented below.

Previous reports of extended explorations of SERS intensities include some of the following: (1) a designed interaction of amino acids with gold NPs;[57] (2) an optimization of photothermal ablation therapies;[55] and (3) a kinetically limited setting using biotin/avidin obtained from larger aggregation responses, where maximum SERS intensities were modeled by the methods of electrodynamics with DLVO/DLS calculations from small clusters i.e.: dimers and trimers were also obtained.[58]

5.2 Micro-Titration Setup

Spectroscopic titration experiments are conducted by serial additions of small aliquots of SERS label, via micropipette, into a stirred cuvette (Figure 12). The protocol

synthesis uses a 1.00 mL of freshly prepared NP solution diluted into an equal volume of

UPW into a sterilized silica cuvette.[50,51] Absorbance and SERS spectra are recorded

concurrently in one minute intervals and followed by addition of each SERS label (i.e.,

R6G, MPY etc.) in separate series. Each label process requires a dedicated set of

pipettors (Fisher Pipetman) and new tips to avoid contamination and to improve

reproducibility of experiments.

Titrations comprise a series of injections of 2.0, 3.2, 5.0, 8.0 and 12.6 μL

respectively for each titrant solution in increasing order of concentration, 1.0, 10, 100,

1000 and 10,000 μM. These specified volumes were pipetted into a 2.00 mL (1 mL

Au@Ag with 1 mL UPW) quartz cuvette (at high stirring) during the course of the

acquisition of the series of Raman and extinction spectra.

Application of these protocols generates a series of concentrations that range from

1 nM to 250 μM in a sequence of 25 steps which produces a log-linear series of

increasing quantities of label with only a small total volume change according to Table 2.

Also, these titrations were designed to cover a large range in analyte concentration (5

orders of magnitude) starting at 1 nM and ending at 250 μM.

Table 2. Universally applied order of addition in a titration with R6G, MPY, or MBA.

						[KCl]	A	B	C	D		E	F	G	H	I	J	K	L
	LABELS FIRST					uL added	0	4	2	4		10	20	20	40	20	20	20	20
	pH = 3.89					Soln (mM)	100	100	100	100		100	100	100	100	100	100	100	100
	Cond = 324 μ s					mM	0	0.2	0.1	0.2		0.5	1	1	2	1	1	1	1
	T = 11.4 C						0	200	300	500	final C (mM)	1	2	3	5	6	7	8	9
	Labe	label vol (uL)	label conc mM	uL	final conc (uM)														
	A	0.0	-		0.0000		AA*	AB	AC	AD		AE	AF	AG	AH	AI	AJ	AK	AL
uM	B	2.0	0.001	2.00	0.0010		BA*	BB	BC	BD		BE	BF	BG	BH	BI	BJ	BK	BL
	C	3.6	0.001	5.54	0.0028		CA*												
E	D	6.3	0.001	11.81	0.0059		DA*	DB	DC	DD		DE	DF	DG	DH	DI	DJ	DK	DL
	E	11.2	0.001	22.86	0.0114		EA*												
	F	2.0	0.010	4.26	0.0213		FA*	FB	FC	FD		FE	FF	FG	FH	FI	FJ	FK	FL
D	G	3.6	0.010	7.76	0.0388		GA*	GB	GC	GD		GE	GF	GG	GH	GI	GJ	GK	GL
	H	6.3	0.010	13.95	0.0697		HA*	HB	HC	HD		HE	HF	HG	HH	HI	HJ	HK	HL

5.3 Diagnosis of Gold Core Synthesis

The extinction measurements of the gold cores were recorded using a Cary-50 Bio with a 200 – 1000 nm (where λ_{MAX} was typically expressed between 520 – 526 nm) which approximated to a particle with a diameter between 17 – 65 nm (Figure 13). Prediction of the Au@Ag NP spectra can be done using the Mie solutions[50,53,59] and the dielectric function can be used to determine the thickness-dependent blue shift in the dipolar plasmon bands.[60] The absorbance peaks are characteristic of the dipolar plasmon resonance of the spherical particles, where the peak magnitudes and λ shifts (bottom left series) are used to identify if the NPs were synthesized properly.
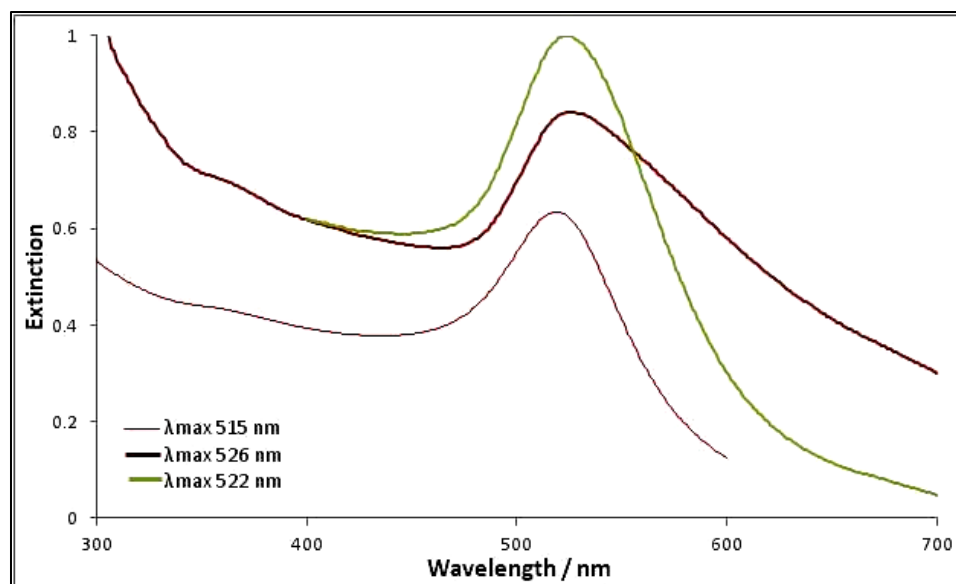
Figure 13. Benchmark of silver/shelling in gold cores by extinction coefficient.

The peak magnitudes and wavelengths are indicative of the silver-shelling

encapsulation which makes it an excellent diagnostic tool of a successful NP synthesis.

Next, the silver shell encasing was determined according to the most intense activity of

the gold core synthesis. This study applied the protocol produced Au@Ag nanoparticles

of predominantly spherical shape with a diameter of ~37 ± 5 nm (shown below in high

resolution TEM images, courtesy of SJSU Professor Folarin Erogbogbo at the UCSC

MACS Facility, at NASA-AMES Figure 14).[51]
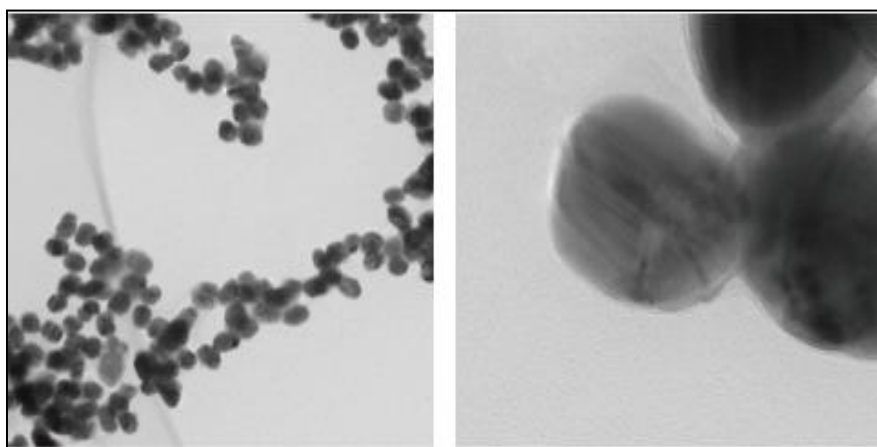
Figure 14. High resolution TEM images of Au@Ag NPs with diameters ~37 ± 5 nm.

49

5.4 Test for SERS Activity in Freshly Prepared Au@Ag NPs

All solutions were benchmarked for SERS activity using R6G at the time of preparation and before other experimentation in order to ensure consistency.[50,51] The spectral positions of the peaks are consistent with those of R6G,[61] 4-MPY,[62] and 4-MBA.[63] In order to check the absorbance properties of the Au cores, a sharp SERS intensity peak activity was recorded from: (1) a blank sample Au@Ag NP (blue spectrum) and (2) a Au@Ag NP aqueous solution treated with 3.4 µL of R6G stock solution (red spectrum) as seen in Figure 15.
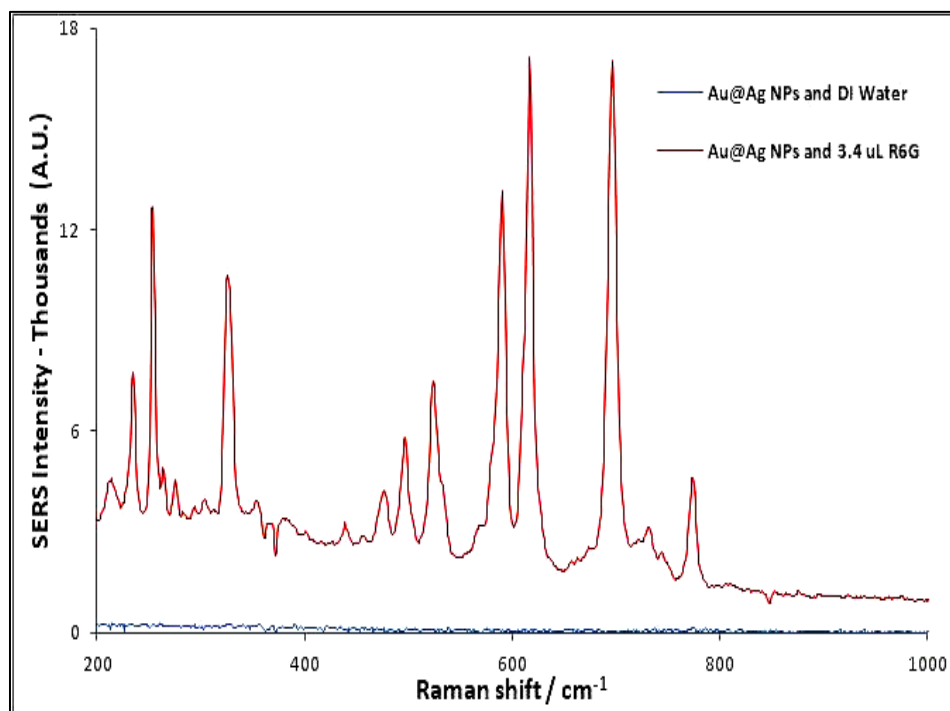
Figure 15. SERS intensity test of Au@Ag core-shell NPs at 0 and 1.5 µM (red) R6G.

PART SIX: FUNDAMENTALS

6.1 General Micro-Titration Procedures

An optimal SERS signal was also achieved for the other two SERS labels according to the protocol below. It is believed from the specific system that SERS signal –SERS produced by Au@Ag and excited with a 750 nm laser light–, comes exclusively from NP aggregates. To determine an optimal detection of enhanced SERS the following steps were followed: (1) using the SERS detection setting where KCl is added first, (2) using the KCl detection setting where SERS label is added first, and (3) find the minimal amount from either (1) or (2) where the optimal SERS signal is triggered. Therefore, an initial setting with an aqueous Au@Ag NPs KCl a micro-titration using a SERS label (i.e., R6G)is then started. At any point in the plane, finding the enhancement of SERS signal may also be achieved for the other two SERS labels using the same protocol.

Under these conditions, aggregation can be triggered either by cationic ligands (i.e., SERS labels) or by KCl. It is possible to find out the type of combination of label and KCl that makes this optimal detection by visualizing a two-dimensional (2D) plot of [KCl] versus [Label] with a [KCl] = 0 to 10 mM, and a [Label] = 0 to 10 μM. On this 2D plot, each point would act as a valid point to test for SERS activity. Figure 16 represents a grid to pick points from the added [Label] and [KCl] in a 2D-surface (square symbols).
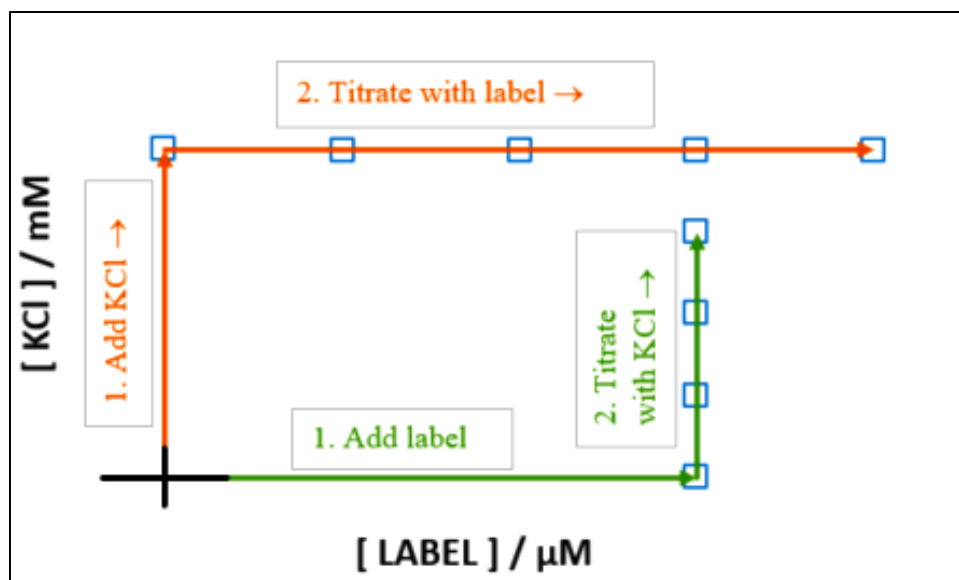
Figure 16. Schematic to describe the μ-titrations. Type 1 (green) label-first (i.e., R6G) is added to the NP solution, and type 2 (orange) the titration starts by addition of KCl-first.

The SERS signal produced at any point in the 2D plane is achieved by either adding KCl before SERS label or vice versa. Then, the SERS and visible wavelength (VIS) spectra were performed by following each addition in the titrations of Au@Ag NPs using the SERS labels that follow: R6G (Figure 17), 4-MPY (Figure 18), and 4-MBA (Figure 19).
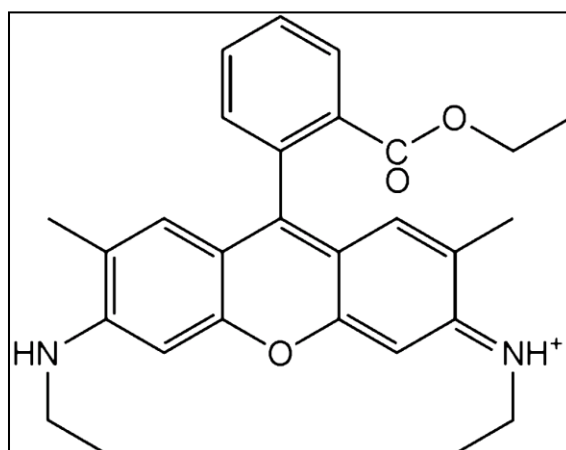
Figure 17. Rhodhamine-6G (R6G) label #1 used in the micro-titrations of Au@Ag NPs.
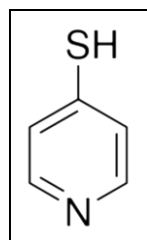
Figure 18. 4-Mercaptopyridine (4-MPY) label #2 for μ-titrations of Au@Ag NPs.
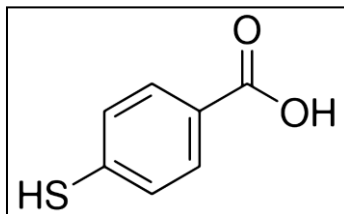
Figure 19. 4-Mercaptobenzoic acid (4-MBA) label #3 for μ-titrations of Au@Ag NPs.

These additions also involved the aggregant potassium chloride (KCl).

Throughout each micro-titration the scheme from Table 3 was followed. This table was

the guidance for each NP solution that was titrated with either SERS label of KCl. This

process was allowed to run for 1 minute under continuous stirring while the spectral from

the solution was recorded.

Table 3. A guide to the interpretation of spectral summaries in Figures 20 and 21 that also
apply to Figures 22 through 27.

Column & Figure:	Name Given to Exp. Series:	NP's Mixed First with:	Mixture Titrated with:
Left Col./ 20	R6G-First KCl	R6G	KCl
Left Col./ 21	KCl-First R6G	KCl	R6G
Center Col./ 20	MPY-First KCl	MPY	KCl
Center Col./ 21	KCl-First MPY	KCl	MPY
Right Col./ 20	MBA-First KCl	MBA	KCl
Right Col./ 21	KCl-First MBA	KCl	MBA

The visible absorbance spectra were acquired simultaneously with SERS spectra by an absorbance spectrometer that was locally supported by Dr. Terrill.[51] Each titration was started with a red spectrum (λ_{MAX} ~515 nm) of pristine Au@Ag solution and as more titrant was continuously added (it was expected that the color of the aqueous solution shifts first from a green to a blue color). This color change can be referenced directly to the label concentration by using an inset that appears in the optical extinction graphs in Figures 22 and 23.

6.2 Report Layout

The results from this study are displayed in groups of 3 graphs in four stages: one, show the SERS intensities (Figures 20 and 21); two, display the optical extinction (Figures 22 and 23); three, contain the integral SERS intensities (~1500 cm^{-1}) along with the extinctions of the aggregated Au@Ag NPs (~830 nm) versus SERS label in[μM] (Figures 24 and 25); and four, represent the calculated linear correlation between SERS versus extinction (corrected ~860 nm) in NPs around [KCl] (Figures 26 and 27).

The graphs contained in Figure 20 display the results from the independent additions of each of the SERS labels of: R6G (right column), 4-MPY (middle column), and 4-MBA (left column) which is also applicable to subsequent graphs on Figures 21 through 27. Another distinction is the spectral analyses from the label-First-KCl micro-titrations belong to Figures 20, 22, 24, and 26 and the one from the KCl-First-label micro-titrations belong to Figures 21, 23, 25, and 27.   Note that the graphs on the left column of Figures 20, and 21 are the only ones showing the labels on the y-axes but do apply across the graphs in the center and right columns. The same method applies to the labels on the x-axes on the bottom graphs across the graphs in the top and middle rows.

PART SEVEN: RESULTS AND DISCUSSION

7.1 Raman Spectra from Micro-Titrations with SERS label–First–KCl

The most relevant results from the R6G-First-KCl SERS micro-titrations were obtained from the [R6G] of 0.22, 0.70 and 2.2 μM and are plotted in the left column of Figure 20. Likewise, the relevant spectral results from the MPY-First-KCl SERS micro-titrations were obtained from the [MPY] of 0.12, 0.70 and 2.2 μM are plotted in centered column of Figure 20. Lastly, the most relevant results from the MBA-first-KCl micro-titrations were obtained from the [MBA] of 1.2, 3.3 and 6.9 μM and are reported in the right column of Figure 20. With the exception MBA additions, the relative SERS band intensities remained roughly constant throughout all the additions of KCl.

However, an onset of the SERS signals was recorded around [R6G] 1.0 uM in KCl-free solutions.[50,51] In general, the spike signals were observed around [R6G] of 0.040 μM and after a [KCl] of about 12 mM was added. These results immediately indicate that a 25-fold improvement in detection limit for R6G in a KCl matrix had been reached, when compared to previous results.[51] Through these runs, it was also noticed that SERS intensities were completely independent of label concentration around the range of 0.20 to 2.0 μM R6G and that by a narrow margin, the peak value (represented as red pointed peaks in middle row of Figure 20) were produced at a [R6G] of 0.70 μM and a low [KCl] of 2.0 mM.

On the other hand, the peak SERS intensities from the lowest [MPY] showed a signal that declined steadily. Soon after an initial addition of [KCl] of about2.0 mM, a moderate and increasing SERS signal was evident at a [MPY] of 0.70 μM. However, this trend stayed constant until a [KCl] of about 30.0 mM was reached. After which the

signal increased sharply as [KCl] exceeded ca. 40 mM. This trend was consistent with

the strong NIR aggregate band. Detection of SERS intensities was obtained at the

following [MPY]: (1) at 0.001 μM (first injection) which showed a continuing peak; and

(2) at 0.20 μM which grew continuously followed by a gradual declined thereafter.

Oddly, the SERS signal was significantly lower, at the highest initial [MPY] than in the

measurements during a low [MPY].

In many ways, the MBA-first-KCl titrations are typical of MBA SERS spectra,[51]

At this stage the SERS intensities reached about a 10% of the total magnitude at its

minimum [MBA] of 1.2 μM. Noteworthy, the strongest SERS intensity for a [MBA] of

1.2 μM at a [KCl] of 20 mM and the intensities that followed were kept lowest among of

all SERS spectra analyses shown at the right column of Figure 20.
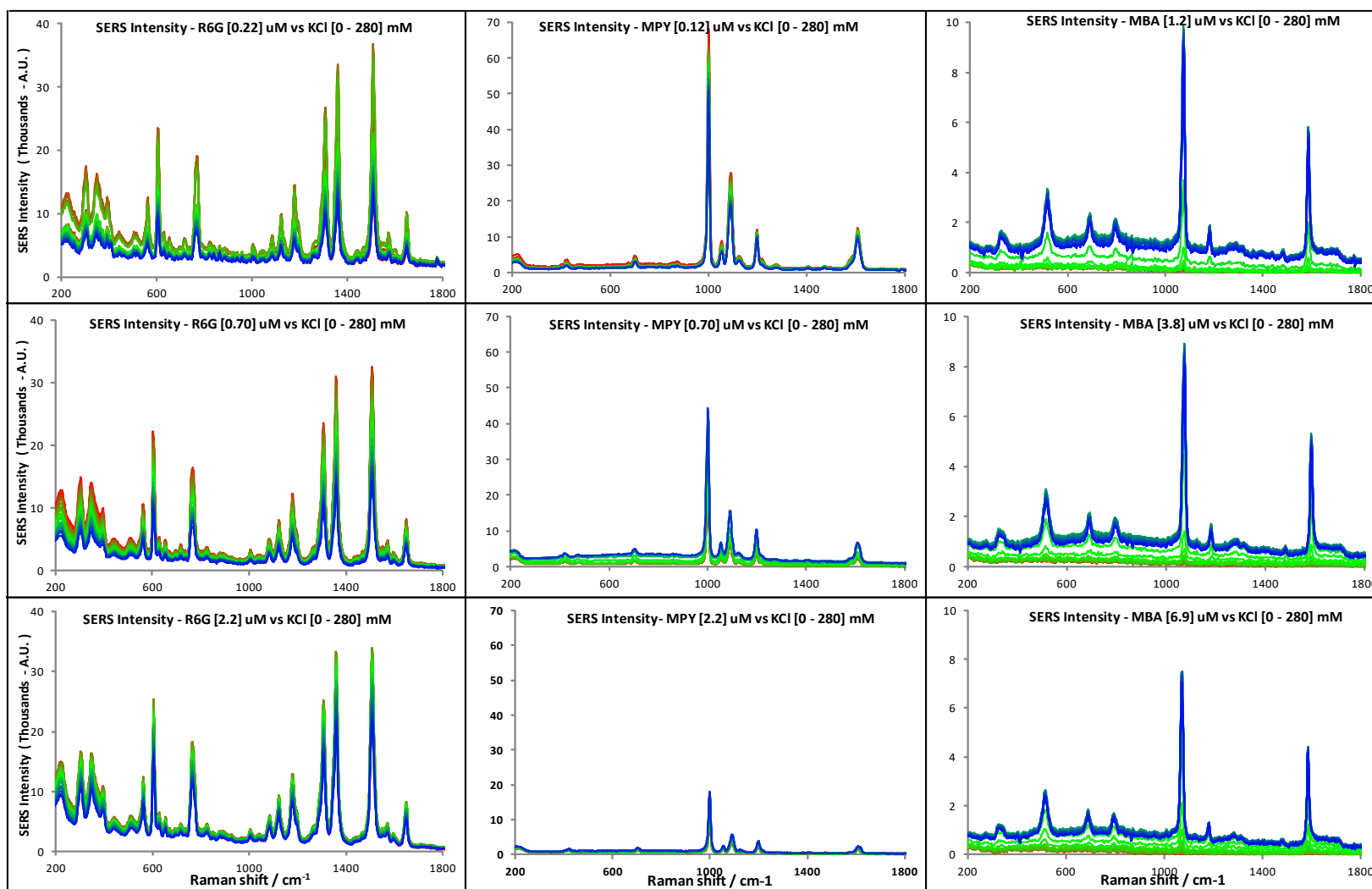
Figure 20. Label-first-KCl Trends of SERS intensities from absorbed SERS labels onto monomeric Au@Ag NPs. Micro-titrations were performed with a [KCl] between 0 – 280 mM with a comparison from [R6G] (left column), [MPY] (center column), to [MBA] (right column).

7.2 Raman Spectra from Micro-Titrations using KCl–First–label

The relevant SERS signals from the KCl-First-R6G titrations of the SERS intensities were obtained when the [KCl] was around 2.0, 5.0 and 10 mM and were followed by additions of [R6G] from around 0 – 2.2 uM and the results were plotted in the center column of Figure 21.

The SERS signals were absent during low additions of [R6G] and they only appeared at the highest end of the concentration axis or roughly at [R6G] of 0.1 μM and soon after a higher [KCl] was reached, it led the SERS signal to a slightly lower limit of detectability as it is shown along the [R6G] axis (left column in Figure 21). During the parallel recording of both spectra, the maximum peak from the aggregate NIR extinction closely trailed the maximum peak in R6G-SERS intensities (~1380 cm^{-1} mark).

As far as the KCl-First-MPY titrations, the SERS intensities followed a less predictable trend. While a pre-addition of KCl had little effect on the subsequent micro-titration of Au@Ag when MPY was added, a simlar trend to that of KCl-First-R6G micro-titration was captured. At first, during the addition of MPY the enhanced SERS grew gradually, but it went up fast at about a [MPY] of 20 μM. As in prior trials, the SERS signal tracked the aggregate band closely in both rising and falling regimes and this shows a correlated pattern between them.

On the other hand, the KCl-first-MBA titrations were extremely weak. This is seen in the two selected graphs where the SERS intensities were not evident. The bands have a downward trend even after more MBA was added. These results are reported on the right column of Figure 21.
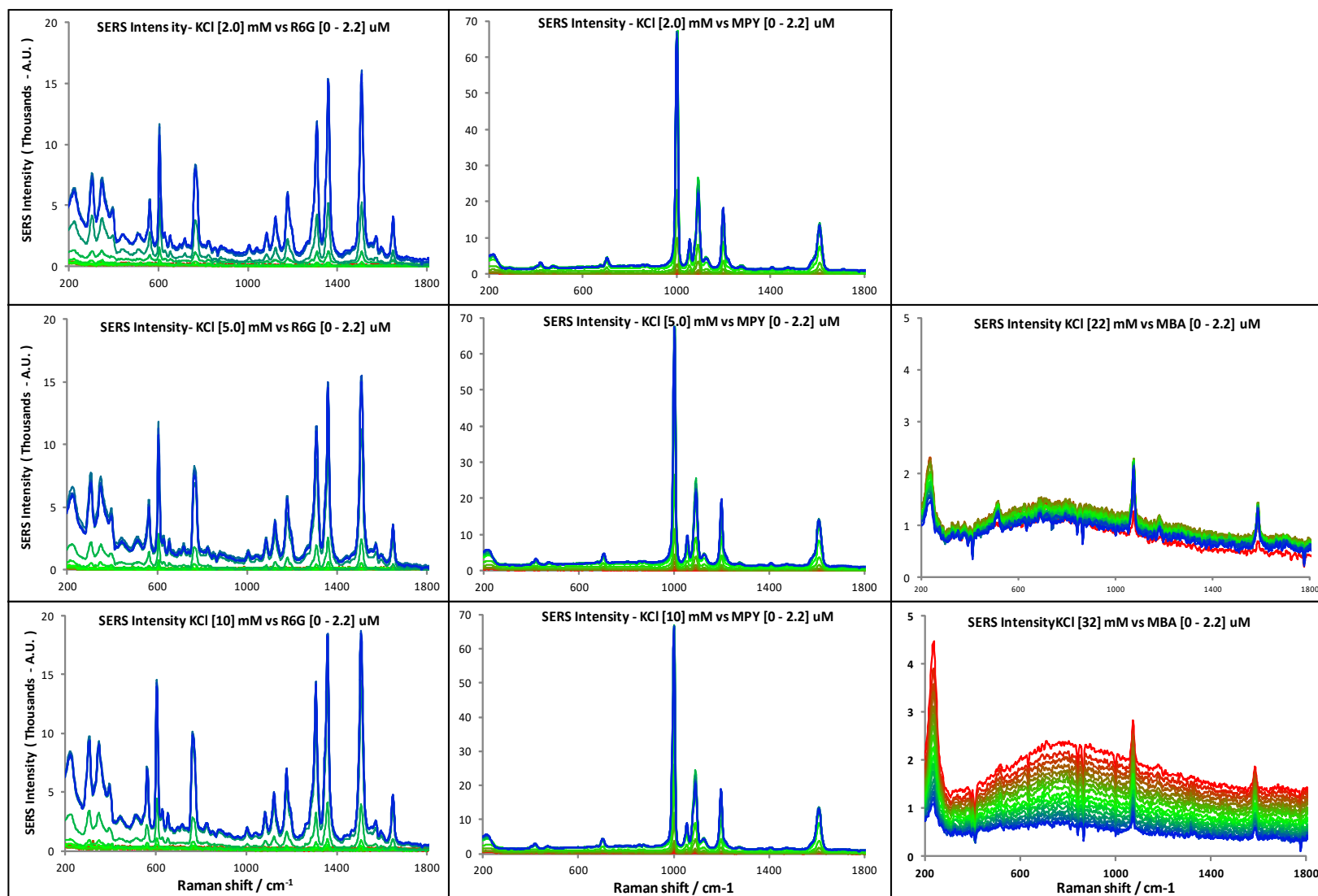
Figure 21. KCl-first-Label Trends of SERS spectra from inital addition of [KCl], between 2 – 10 mM with a comparison from [R6G] (left column), [MPY] (center column), to [MBA] (right column) which was obtained from a [22] (middle row) and [32] mM (bottom row).

7.3 Extinction Spectra from Aggregated Au@Ag from Label-First-KCl

Trends of visible spectra from LSPR on individual (λ_{MAX} ~ 500 nm) and aggregated Au@Ag (λ_{MAX} ~830 nm) were collected for R6G-first-label at the [R6G] of 0.12, 0.70, and 2.2 μM that were followed by additions of [KCl] of 0 – 280 mM (left column, Figure 22). Next, the visible spectra from MPY-first-label was recorded at the [MPY] of [0.22], [0.70], and 2.2 and were followed by additions of KCl [0 – 280] mM (center column, Figure 22). Likewise, the visible spectra from MBA-first-label followed this same process but the recordings were made at the [MBA] of 1.2, 3.8, and 6.9 μM which were also followed by additions of KCl [0 – 280] mM (right column, Figure 22).

Extinction spectra from aggregated Au@Ag NPs illustrate the aggregation process revealed by the LSPR on Au@Ag NPs.[50,51] Evidence of the absorbance of laser light by the monomeric Au@Ag NPs is represented by a peak formation at around 500 nm at the left end of the graphs of Figure 22.

Aggregates that absorb in the NIR range created a peak near the 800 nm mark. This spectral position occurs where other experimental factors become dependent on. It occurs as soon as the signal is red shifted by the aggregation of Au@Ag .[50] Normally, a rising NIR extinction is accompanied by a corresponding decline in intensity at about 515 nm produced by a dipolar plasmon band. This process creates a visible orange to gray/blue color transition in the solution and it is evidence that aggregation has occurred. In turn, the SERS signals that arise in this setting are a direct product of label interaction with the aggregate structures.

Figure 22. Label-First-KCl Trends of visible extinction spectra from LSPR on individual ($\lambda_{MAX} \sim 500$ nm) and aggregated Au@Ag ($\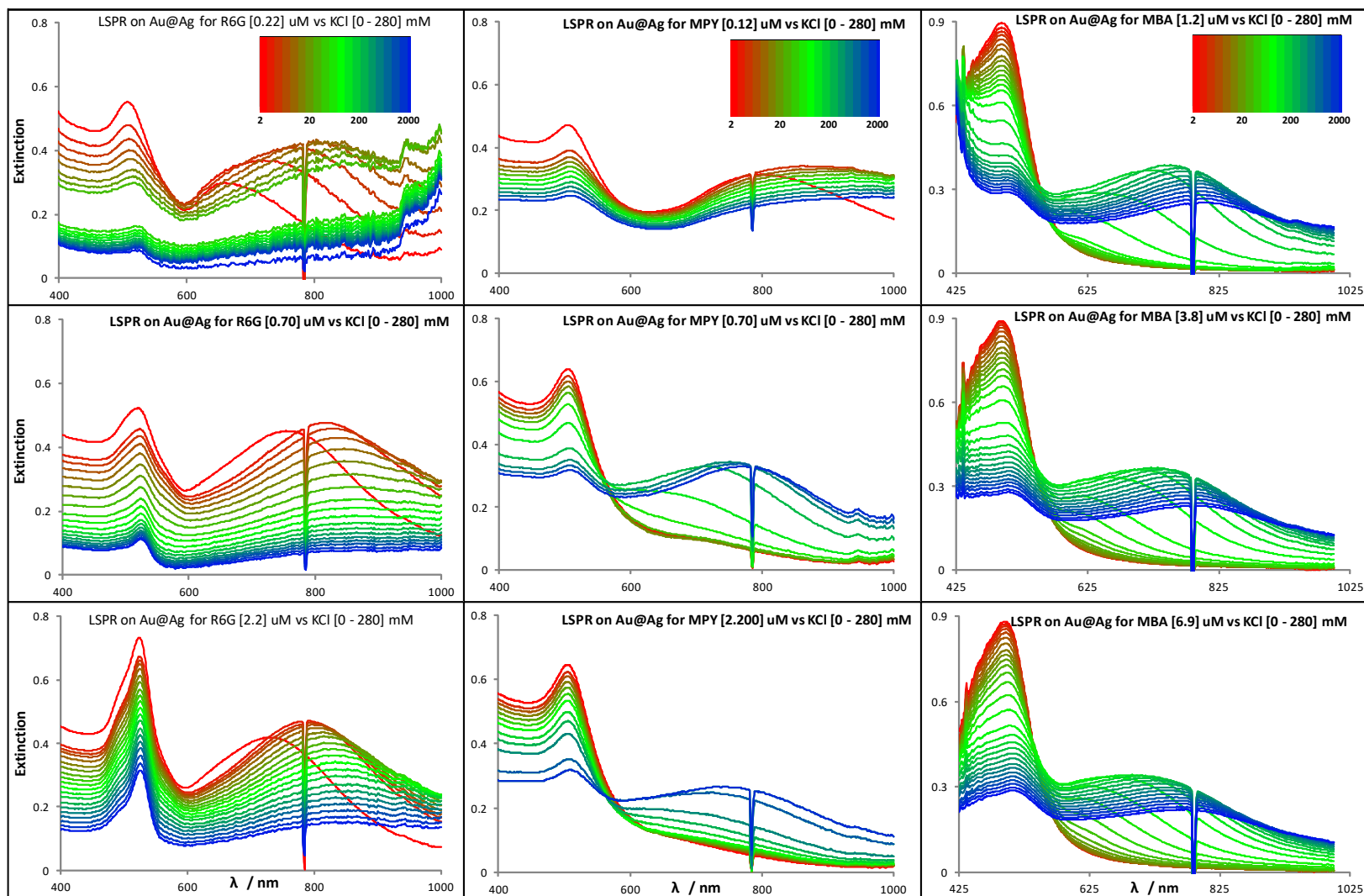lambda_{MAX} \sim 830$ nm) with color coded concentrations from 1 nM (red bands) to 1 mM (blue bands) for [R6G] (left column), [MPY] (center column), to [MBA] (right column). The break in the extinction at ~785 nm is due to the laser light.

7.4 Extinction Spectra from Aggregated Au@Ag from KCl-First-Label

Trends of extinction spectra from the KCl-first-R6G micro-titrations are presented in the left column of Figure 23. It shows that from the initial additions of [KCl] the SERS signal remains unchanged even when the R6G started to be added. It may be asserted that the shape of the R6G molecule has sites that may be chemically neutralized by the presence of KCl, but this effect is not permanent since it can act like an off and on switch. This was differentiated after the initial addition of R6G when no aggregation of Au@Ag was seen. Soon after more R6G was added the SERS intensities were immediately enhanced or were turned on by the switch of aggregation form R6G which occurred with as little as a [KCl] of 2.0 mM and after a [R6G] of 60 μM was added.

This trend is more settled during the KCl-first-MPY micro-titrations and this is evident in the changes of the spectral bands. The blue bands that gathered at the top of the plot occurred during the initial order of additions of MPY, but around the middle additions of MPY the aggregation event was triggered. It is possible that the KCl competes with the charges around the thiol group of the MPY molecule and aggregation only occurs until enough MPY has been added which is when aggregation is unlocked.

Conversely, the effect from KCl over the addition of MBA that is shown at the right column of Figure 23 has a stronger effect than those from R6G and MPY. However, in this case there was no apparent trend of aggregation. The anionic character of MBA does not trigger aggregation alone hence it behaves quite differently than R6G or MPY. Therefore, MBA is entirely dependent on the aggregating effect of KCl for detection of an aggregation of Au@Ag.
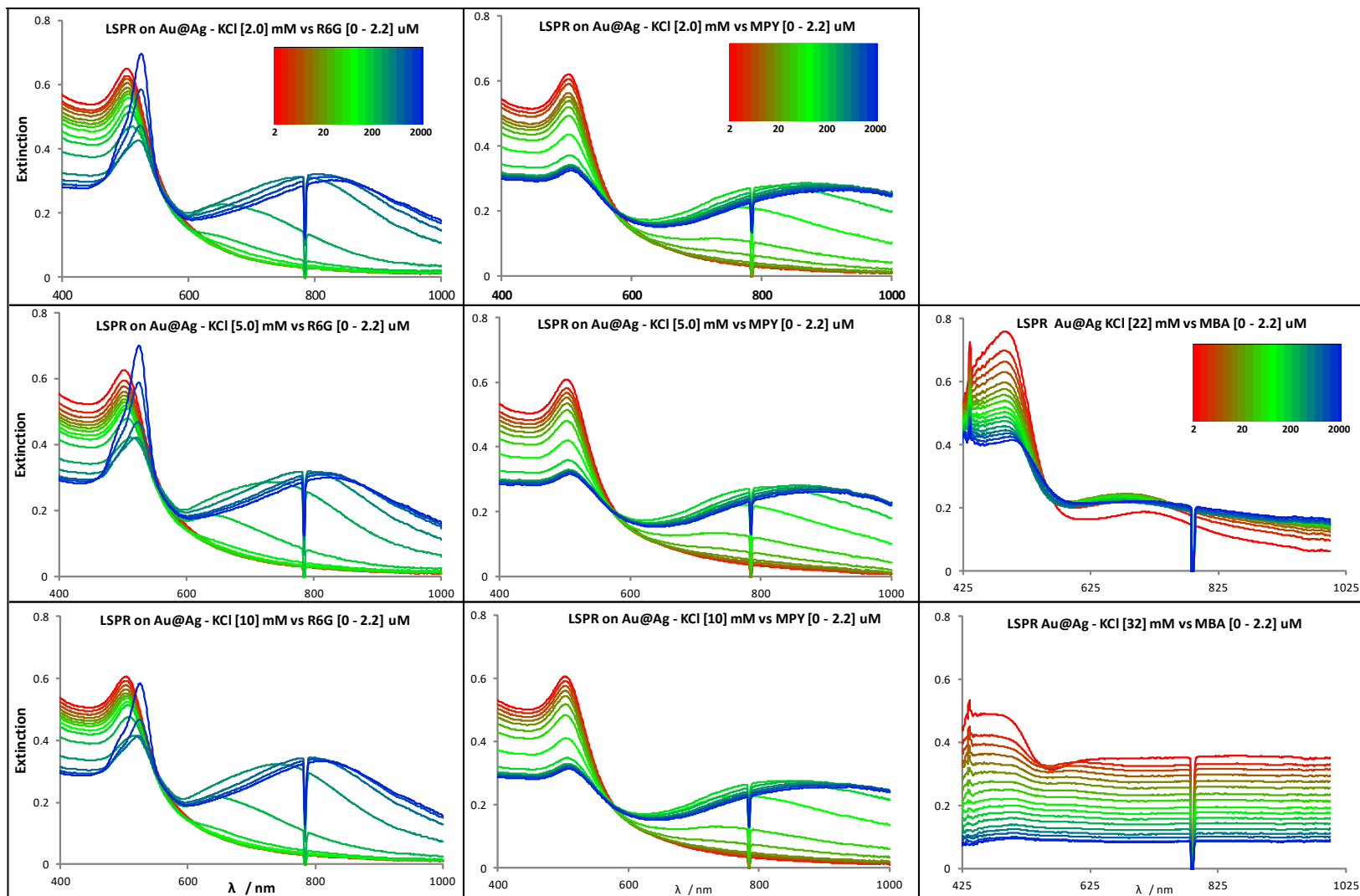
Figure 23. KCl-first-Label Trends of visible extinction spectra from LSPR on individual (λ_{MAX} ~ 500 nm) and aggregated Au@Ag (λ_{MAX} ~830 nm) with color coded concentrations from 1 nM (red bands) to 1 mM (blue bands) for [R6G] (left column), [MPY] (center column), to [MBA] (right column). The break in the extinction at ~785 nm is due to the laser light.

7.5 Integral SERS Intensities versus Optical Extinction by Label-First-KCl

The linear correlation between SERS versus extinction (corrected ~860 nm) in NPs from the label-first-KCl micro-titrations are reported in Figure 24. The trends from these graphs revealed that if significant changes could not be observed on stages one and two, they may be identified from these plots.

From these results, there is well marked enhanced SERS from the titration with the SERS label of R6G and MPY (left and right columns respectively). This does not weight in the same proportion for the plot from MBA. Observation of the integral SERS versus the optical extinction from MBA clearly shows that while there is a sudden rise for the band from LSPR signal, the SERS signal is not significant. In contrast to the R6G and MPY runs, the integral SERS and the optical extinction do follow each other which may be correlated to the enhancement of SERS intensities by the LSPR on the aggregated Au@Ag. Obviously, an analysis with the use of the theories stated above may give a better insight of these results.

Figure 24. Label-First-KCl Trends of Integral SERS intensities (~1500 cm^{-1}) along with the extinctions of the aggregated Au@Ag NPs (~830 nm) versus KCl [mM] for [R6G] (left column), [MPY] (center column), to [MBA] (right column).

7.6 Integral SERS Intensities versus Optical Extinction by KCl-First-Label

The linear correlation between SERS versus extinction (corrected ~860 nm) in NPs were recorded from the KCl-first-label micro-titrations and reported in Figure 25. In this Figure, the corrected SERS intensities are plotted against the corresponding aggregate extinction data (measured at 830 nm). The protocol is the same for R6G (left column), MPY (center column) and MBA (right column) and were followed with KCl.

The trends from the integral SERS intensities versus the optical extinction from MPY (center column) show a better match than those from the R6G and MBA plots. In the case of R6G, a faster rise of the optical extinction trend versus the integral SERS intensities also suggest that there is a possible correlation between the enhanced SERS intensities and the LSPR on aggregated Au@Ag. Conversely, the signals from the MBA plots do not show a significant trend since these originated in the weaker trends from the previous plots from stages one and two. Moreover, the intensity scalar from the y-axis on each of the following plots can be placed in the following order: (1) MPY (which has an intensity magnitude of about 20,000 times with the one from MBA), (2) R6G, and (3) MBA.
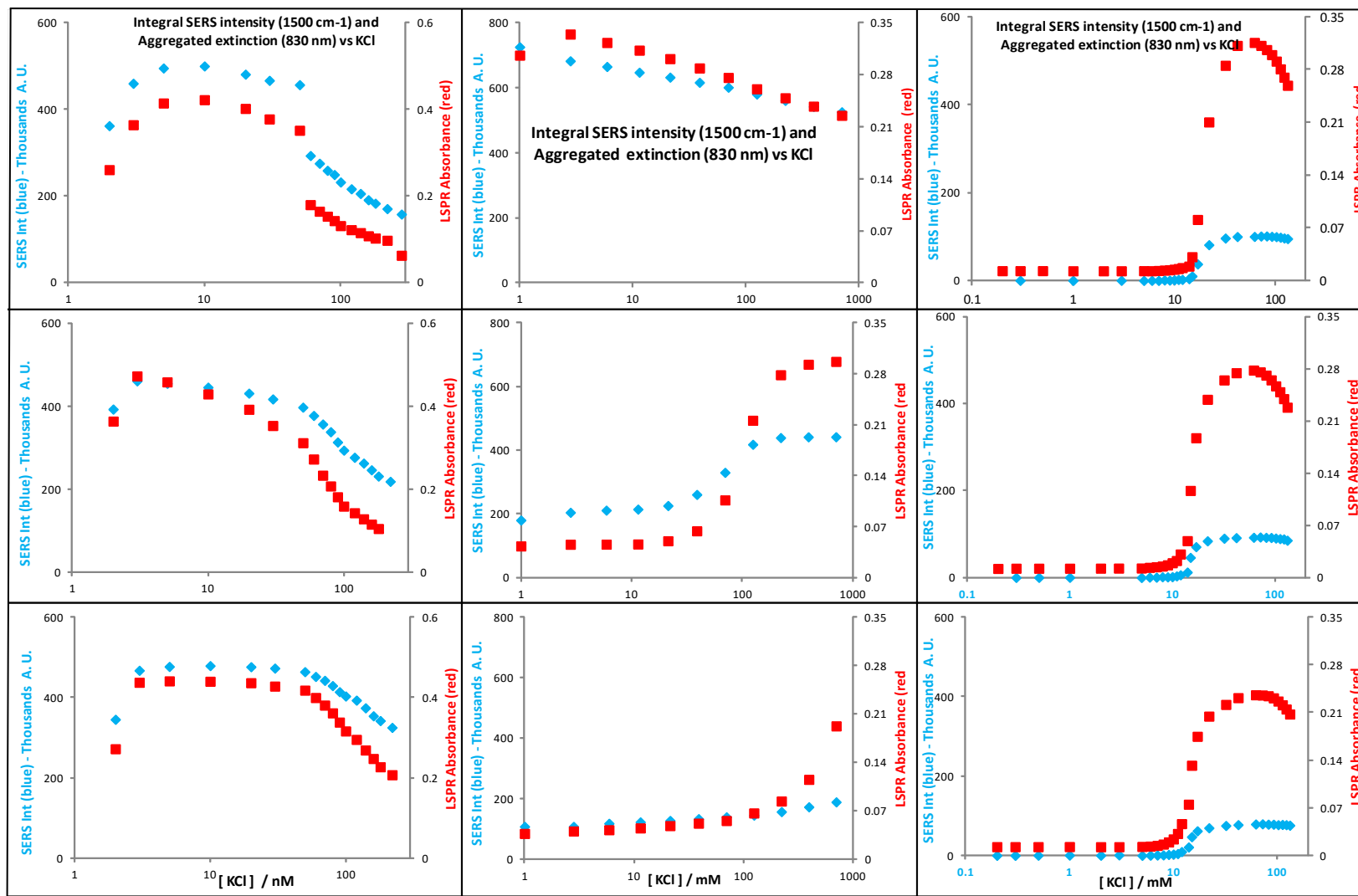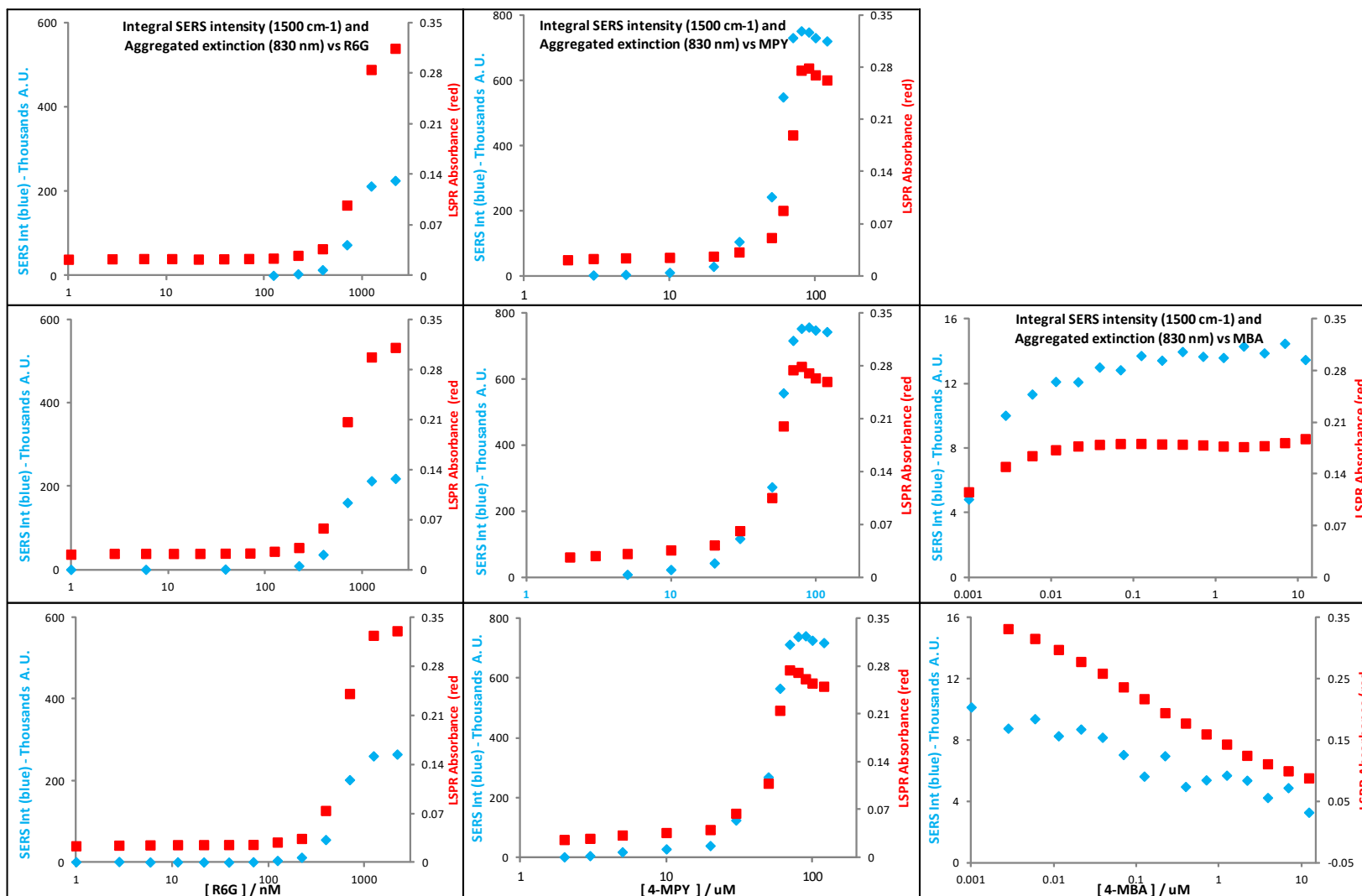
Figure 25. KCl-First-Label Trends of Integral SERS intensities (~1500 cm^{-1}) along with the extinctions of the aggregated Au@Ag NPs (~830 nm) versus 4-MBA [μM] for [R6G] (left column), [MPY] (center column), to [MBA] (right column).

7.7 Linear Correlation between SERS Intensity (Corrected for ε at λ~860 nm) by Label-First-KCl and by KCl-First-Label

Each of SERS label-first-KCl (Figure 26) and the KCl-first-label (Figure 27) graphs show the best linear trend which strongly supports a correlation of the enhanced SERS intensities and LSPR on aggregated Au@Ag. These plots illustrate the representative corrected I_{SERS} vs $A_{AGGREGATE}$ (λ ~830 nm) measurements for the three analytes.[51] The corrected SERS signal (using the NP SERS at 860 nm) versus NP extinction at 860 nm shows an excellent correlation in both, ascending and descending extinction trends that are shown in Figures 26 and 27. It is also important that the SERS and absorption data were obtained simultaneously due to the dynamic nature of the aggregation process. This spectral connection is crucial since SERS appear lower at high absorbance by exhibiting a negative deviation from linearity or above A > 0.050-0.10. The striking consistency of Au@Ag SERS -of intense SERS signals-, comes in direct proportion to the aggregate absorption bands intensities that was observed near the 830 nm mark. There are minor changes from these results that need to be addressed like the small displacement that reduces the spanned of the ascending and descending extinction trends as well. Lastly, the careful recordings of these data, that were followed by the extensive calculations with the subprograms from Visual Basic, clearly show the successful linearity that exist between the enhanced SERS and the extinction spectra.
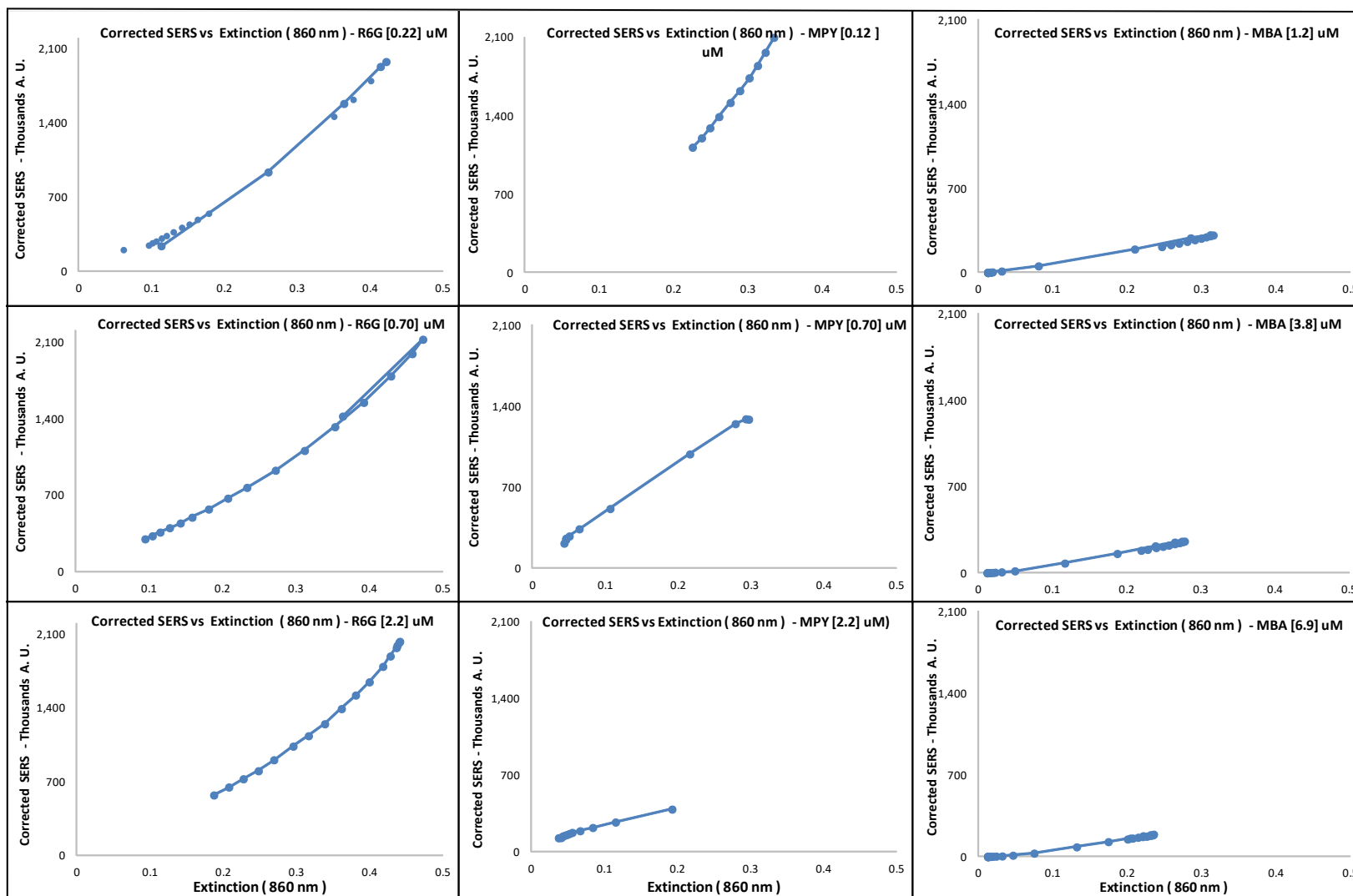
Figure 26. Label-first-KCl Linear correlation between SERS versus extinction (corrected ~860 nm) in NPs around KCl concentrations for [R6G] (left column), [MPY] (center column), to [MBA] (right column).
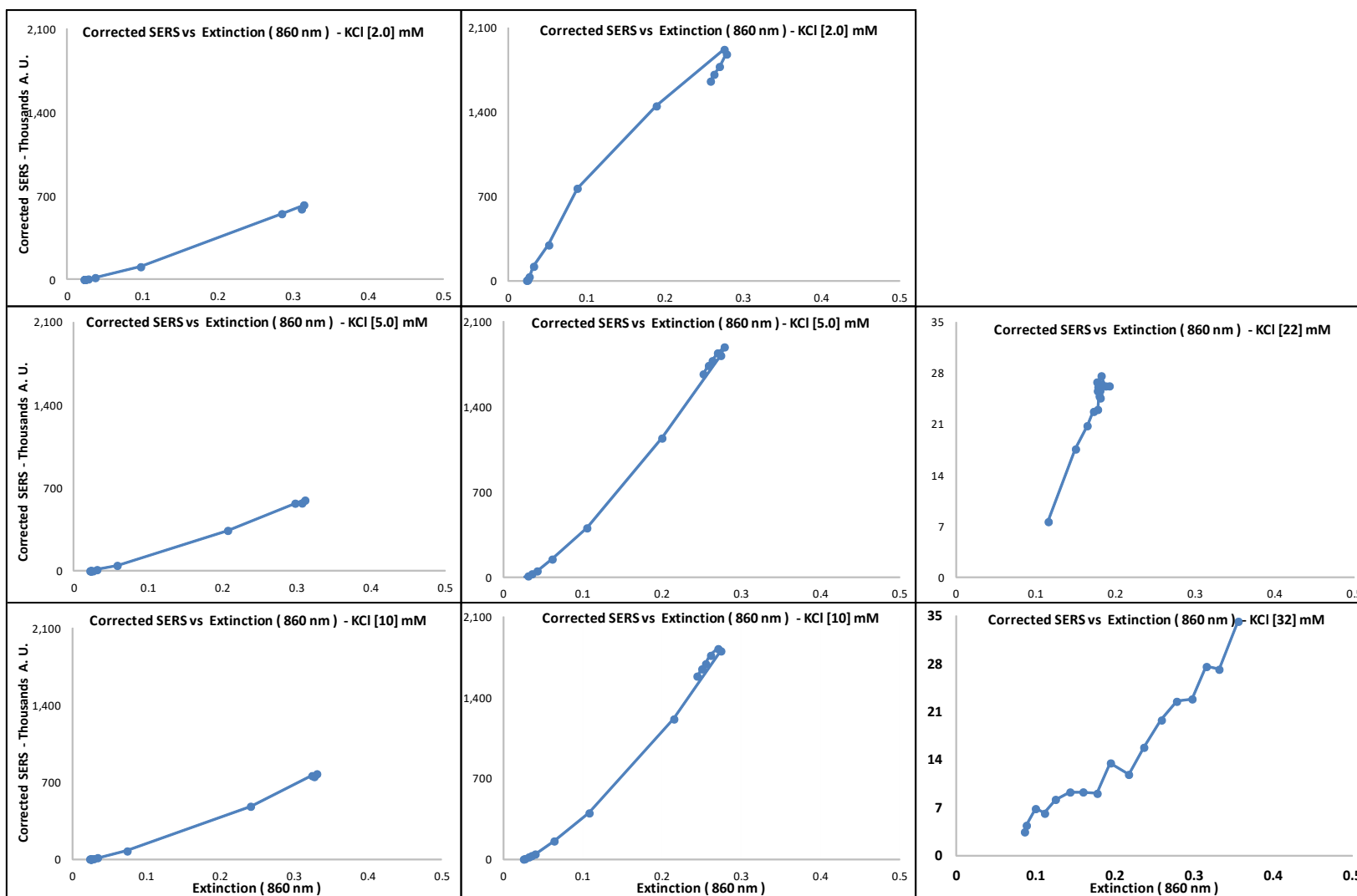
Figure 27. KCl-First-Label Linear correlation between SERS versus extinction (corrected ~860 nm) in NPs around Label concentrations for [R6G] (left column), [MPY] (center column), to [MBA] (right column).

PART EIGHT: COMPLEMENTARY CALCULATIONS

8.1 Enhancement Factor Estimates from SERS Intensity

In order to compute the absolute enhancement factor for the SERS peak previously addressed in equation 3.2.1 is invoked now one more time:[51,98]

$$EF \sim 1.7x10^6 = \frac{I_{SERS}/N_{Surf}}{I_{Raman}/N_{Vol}}$$
3.2.1

where I_{SERS} and I_{Raman} are the integrated band intensities and

N_{Surf} and N_{Vol} are the numbers of molecules interrogated in each setting.[98]

8.2 Absolute Scattering Cross Section from Aggregated Au@Ag NPs

The absolute scattering cross section of this Au@Ag system was estimated by using the absolute cross section of R6G (measured at λ_{EX} = 633 nm, but corrected to 785 nm) as $1.25x10^{-21}$ cm^2 sr^{-1} is calculated below by employing the literature value of 1364 cm^{-1} band of R6G ($1.8x10^{-27}$ cm^2sr^{-1}, measured using l_{EX} = 633 nm) in equation 8.2.1:[51,98]

$$\frac{d\sigma_{SERS}/d\Omega}{d\sigma_{Raman}/d\Omega} = \frac{I_{SERS}/C_{SERS}}{I_{Raman}/C_{Raman}}$$
8.2.1

where $d\sigma_{SERS}/d\Omega$ and $d\sigma_{Raman}/d\Omega$ are the differential SERS and normal cross sections of the R6G band in question that also equate to: I_{SERS}

which are the integrated signal intensities for SERS, and

I_{Raman} which are the normal Raman signals made under identical intensity and integration times.

In the present study, both diffusing particles and R6G label, which produced the SERS and Raman spectra can be represented by equations, 8.2.2 and 8.2.3 as follows:

$$C_{SERS} = \frac{N_{Surf}}{V_{Det}}$$
8.2.2

$$C_{Raman} = \frac{N_{Vol}}{V_{Det}}$$ 8.2.3

where V_{Det} is the same in each case because the detection geometries are identical then it follows that from equation 8.2.1 can be represented within equation 8.2.4:

$$\frac{d\sigma_{SERS}}{d\Omega} = EF \cdot \frac{d\sigma_{Raman}}{d\Omega}$$ 8.2.4

with a normal Raman differential cross sections for the 1364 cm^{-1} band of R6G[96] for $l_{EX} = 633$ nm that must be corrected for the $\sim v^4$ which is the frequency dependence of cross section on excitation frequency given by equation 8.2.5:

$$\sigma \propto v_{EX}(v_{EX} - v_{Vib})^3$$ 8.2.5

where v_{Vib} is the frequency of the Raman vibrational mode.

Thus a correction factor between the 633 nm and 785 nm can be obtained using equation 8.2.6:

$$\frac{\sigma_{785}}{\sigma_{633}} = \frac{v_{EX}^{785}(v_{EX}^{785} - 1364\ cm^{-1})^3}{v_{EX}^{633}(v_{EX}^{633} - 1364\ cm^{-1})^3} = 0.40$$ 8.2.6

Therefore from the absolute cross section of R6G presented in equation 8.2.4 the result is as follows:

$$\frac{d\sigma_{SERS}^{785}}{d\Omega} = 0.40 \cdot EF \cdot \frac{d\sigma_{Raman}^{633}}{d\Omega} =$$ 8.2.4

$$= 0.40 \cdot 1.7_4 x 10^6 \cdot 1.8 x 10^{-27}\ cm^2 sr^{-1}$$

8.3 Shift Magnitude of λSPR from Dielectric Sensitivity to MBA Coating

It can be deduced that the MBA molecules are adsorbing by examination of the LSPR wavelength (λ_{SPR}) as this value is expected to vary as surface adsorption occurs according to the relationship from equation 8.3.1:[50]

$$\Delta\lambda_{SPR} = m\Delta n\ [1 - e^{(-2d/l_d)}]$$ 8.3.1

where m is the intrinsic LSPR dielectric sensitivity,

Δn is the difference in refractive index between the adsorbate and the displaced solvent,

d is the adsorbate layer thickness,

l_d is the evanescent wave penetration depth of the plasmonic field, and when

Δn value approaches a limit the coverage of adsorbate reaches unity.

In reference to Figure 15, the blue triangular symbols indicate $\Delta\lambda_{SPR}$ and clearly reveal the expected Langmuirian red-shift expected for the adsorption of a layer of MBA. This absolute magnitude of the shift cannot be fully evaluated without more experimentation with Au@Ag nanoparticles. But the magnitude of the shift, ca. 1 nm is completely consistent with LSPR shifts for monolayer adsorption.[51]

8.4 Screening of Charges in Solution around Monomeric Au@Ag NPs

MBA SERS spectra on solution phase Au@Ag NPs appear very weak despite the obvious structural similarity to MPY in despite the fact that an intense SERS is reported for MBA under other settings.[51] This is because MBA does not trigger aggregation in as-prepared Au@Ag. Therefore, the very weak SERS signals can be ascribed to monomeric (i.e. non-aggregated) Au@Ag coated with MBA. In this case, the SERS signal from the MBA arises because a simple dipolar (or monomeric LSPR) underpins this phenomenon as opposed to the more intense aggregate-based SERS.

Therefore, aggregation was induced through the addition of KCl to NPs that were pre-treated with [MBA] = 1.7 μM. This concentration corresponds to an approximately complete surface coverage and it was based on the $\Delta\lambda_{SPR}$ signal formula (equation 8.3.1). Next, the pre-coated NP's were titrated with KCl, resulted in the production of intense SERS signals.[99] Usually, these SERS signals were promoted by NP aggregation through

the increasing the solution ionic strength, which in turn screens the mutual repulsive

charges of the NPs. But MBA does not induce aggregation that appeared consistent with

the negative free particle ζ-potential for these particles.[51] Instead, it was the presence of

cationic dye molecules that neutralized the negative potential and triggered aggregation,

while the anionic MBA did not.

8.5 DLVO Applied to Observed Intense SERS in Au@Ag|R6G System

Next, the promotion of NP aggregation happened specifically after the addition of

a [MBA] of 1.2 µM and a [KCl] of 10 mM and it can be described in the form of an

on/off switch. These aggregation effects were observed as a screening of charges in

solution effect. Initially, the NPs are found as monomers immersed in a non-ionic

solution. Then, an addition of MBA to the aqueous solution adds a layer of coating

around the surface of the Au@Ag NPs. This coating is supported by the covalent

properties between the sulfur and the Ag^0 (or a +1 charge) on the surface of the Au@Ag.

The presence of enough $[K^+]$ creates a repelling force V_{Rep} (kT) between monomeric

species. An incremental addition of $[Cl^-]$ that follows counterbalances any repelling

interactions amongst the coated NPs. In accordance to the DLVO theory, the gathering of

enough attractive and repelling forces from the V_{Total} (kT) formula, (equation 3.5.6) that

are produced by the screening of charges in solution, are close or equal to zero. Sooner

than previously reported, the intense SERS signals was obtained observed and recorded

as the LSPR of aggregated Au@Ag NPs caused red signals (Figure 28). Posterior data

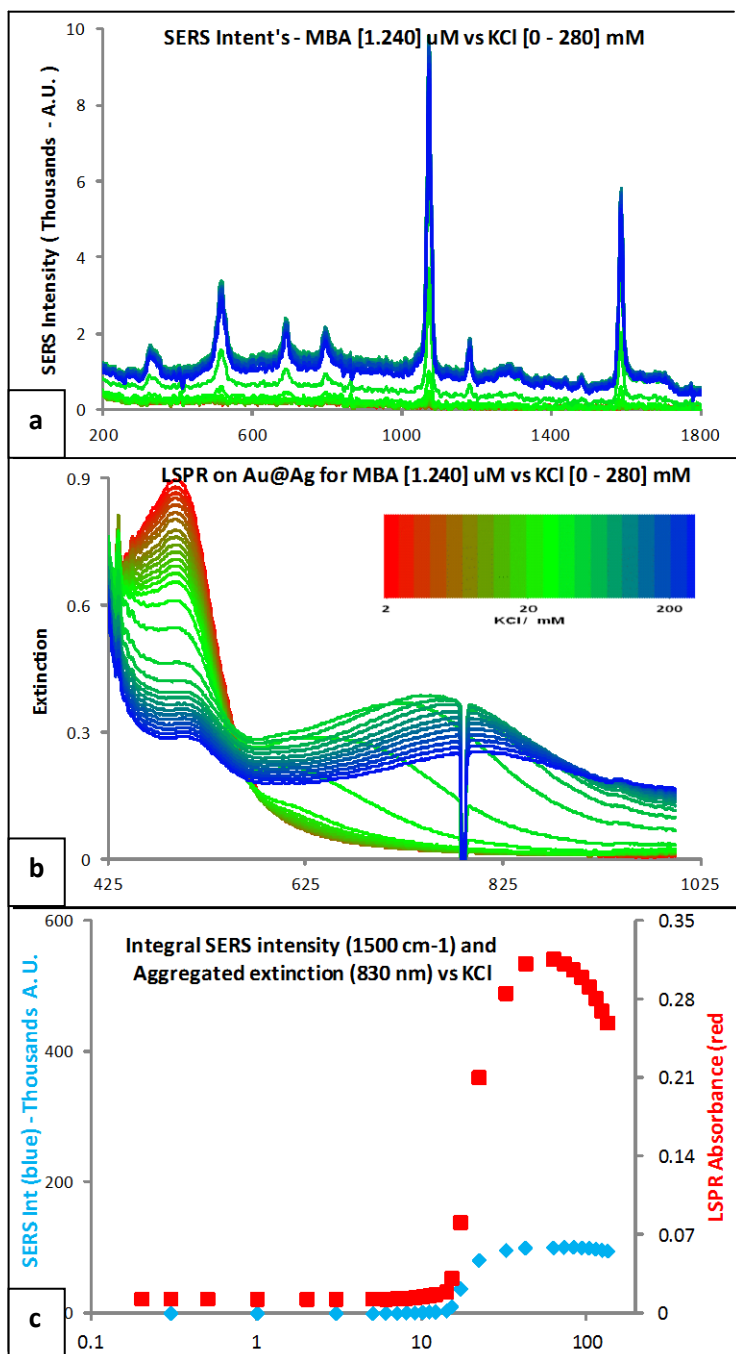analysis allowed the corroboration of the correlation this report supports.

Figure 28. MBA correlated to: (a) the SERS intensity; (b) the extinction spectra; and (c) the Integral SERS intensities vs. aggregated extinction (λ ~830 nm) that were caused by the LSPR from aggregated Au@Ag NPs, but occurred at lesser intensities than previously reported (recorded as intense red signals, bottom).

8.6 Significant Correction of SERS Intensity in Aggregate Extinction

All the above observations suggest that the intense SERS observed is connected to the aggregation state. Since the relative aggregate concentration can be measured approximately by the absorbance in the NIR region, it makes sense to plot the SERS signals as a function of this absorbance. But the SERS intensity data need to be corrected for light attenuation for both the incoming (λ_{EX} = 785 nm) and outgoing (emitted Raman Stokes wavelengths). These corrections to the SERS output intensity were made to compensate for solution absorption of both the λ_{EX}= 785 nm Raman excitation beam and the Stokes shifted emission. These are like those described for the correction of primary and secondary absorption effects in fluorescence spectroscopy that were taken from a standard analytical chemistry text,[100] but were simplified by consideration of emission intensity arising only from the focal point of the excitation laser.

This approximation is justified by the optical configuration of the Raman probe. The collection optics focus the emission from the laser focal point, onto the end of a fiber optic, thereby behaving as a spatial filter and therefore rejects radiation emanating from other points in space within the cuvette. The calculation is facilitated because, in these experiments, we have made concurrent and in-situ measurements of the solution absorption at both: (1) the excitation wavelength, λ_{EX} = 785 nm and (2) the Stokes Raman wavelength, λ_{EM} for each SERS measurement. The focal point of the 785 nm laser excitation beam lies at a point approximately 6 mm within the solution contained in the cuvette. (This consideration includes the 7 mm focal length of the lens tube, minus 1 mm for the cuvette wall, and a small setback between the focusing lens and the cuvette walls). Therefore, it is possible to compute the attenuation of the input laser experienced at the

focal point of the solution, by applying Beer's law as equation 8.6.1 shows:

$$I_x^{fp} = I_0^{fp} \cdot 10^{-\varepsilon_{EM}Cx}$$
8.6.1

where ε_{EM} is the molar absorptivity at $\lambda_{EX} = 785$ nm,

C is the absorber concentration,

x is the path length in solution, and

I_x^{fp} and I_0^{fp} are intensities at the focal point and prior to entering the solution.

The emitted Raman radiation arising from this focus (I_x^{Raman}) is transformed into Stokes Raman emission with a certain efficiency proportional to some power n, of the local excitation intensity. This transformation efficiency is identified as ϕ and it includes various factors related to the physical states of the nanoparticle-label systems. It behaves as a function of added label in the titration experiments. The intensity of the emitting species in the beam focus can be obtained from equation 8.6.2:

$$I_x^{Raman} = \phi \, (I_x^{fp})^n$$
8.6.2

Now the attenuation of this Raman emission x by the solution as it travels from the focus to the collection lens on the Raman probe needs to be considered. This distance is the same as that transited by the excitation beam and the emitted beam is attenuated according to the absorptivity, ε_{EM} at the Stokes (EM) wavelength yielding a measurable intensity (I_0^{Raman}) which are expressed in equation 8.6.3:

$$I_0^{Raman} = I_x^{Raman} \cdot 10^{-\varepsilon_{EM}Cx}$$
8.6.3

This measured attenuated Raman intensity can be related to the emission process at the focus by combining equations, 8.6.3 and 8.6.2 into equation 8.6.4 below:

$$I_{Corr}^{Raman} = \phi \, (I_0^{fp} \cdot 10^{-\varepsilon_{EX}Cx})^n \cdot 10^{-\varepsilon_{EM}Cx}$$
8.6.4

8.7 Corrected Absorption from Corrected Raman Stokes signal of SERS

The next step is to recover all the intrinsic activity term $\phi\ (I_0^{fp})^n$. As the solution is titrated, it becomes more opaque thus allowing the correction of the measured signals by dividing it by the attenuation factors which produce the absorption corrected value (I_{Corr}^{Raman}) of equation 8.7.1:

$$I_{Corr}^{Raman} = \phi\ (I_0^{fp})^n = \frac{I_0^{Raman}}{(10^{-\varepsilon_{EX}Cx})^n \cdot 10^{-\varepsilon_{EM}Cx}} \qquad 8.7.1$$

where the exponents $\varepsilon_{EX}Cx$ and $\varepsilon_{EM}Cx$ are derived directly from the concurrent acquired extinction measurements from the SERS and the NIR visible spectra. The power dependence of SERS emission n is assumed to be 2 and it is consistent with current $|E|^4$ models of plasmon field enhancement of the incident and emitted beams.[101]

A summary of linearity from the corrected I_{SERS} versus $A_{AGGREGATE}$ (λ_{ABS} ~830 nm) measurements for R6G (red trend line), 4-MPY (blue trend line), and 4-MBA (green trend line) is illustrated in Figure 29. Note that it is important that in acquiring the SERS and absorption data must be simultaneously due to the dynamic nature of the aggregation process. The spectral correction is crucial because without it, SERS are lower at high absorbance and by then it would exhibit a negative deviation from linearity A > 0.05.
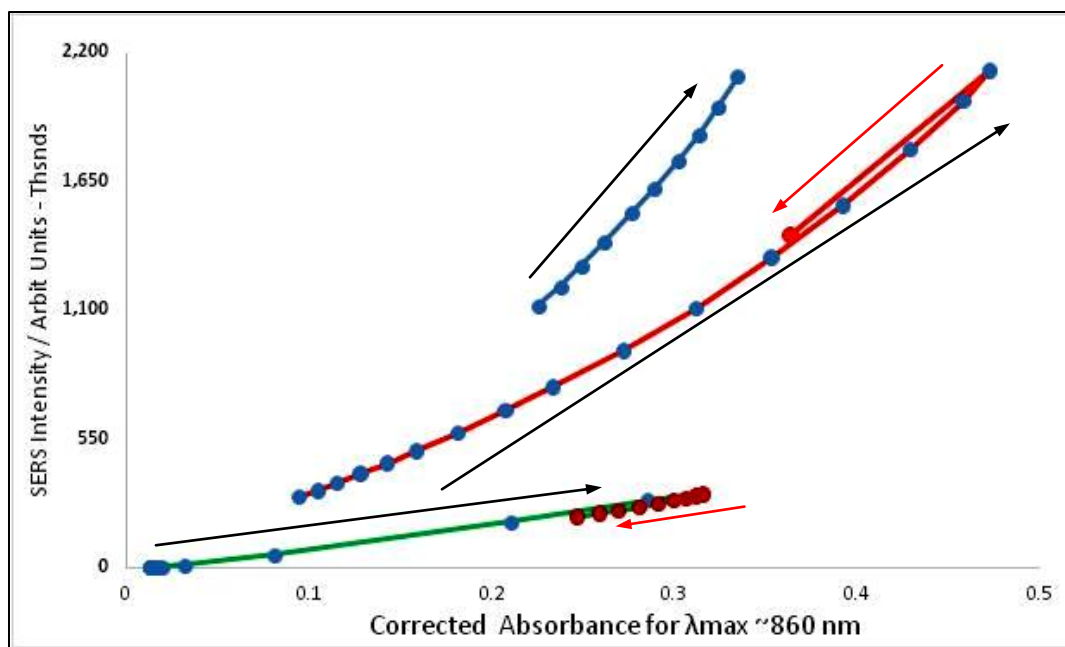
Figure 29. Representation of corrected SERS intensities versus the corresponding aggregate extinction data (corrected for λ_{MAX} ~860 nm) for R6G (red trend line), 4-MPY (blue trend line), and 4-MBA (green trend line).

Also, Figure 29 summarizes one of the more strikingly consistent aspects of Au@Ag SERS found in these experiments that the intense SERS signals in this system occur in direct proportion to the aggregate absorption bands intensities corrected for λ_{MAX} ~ 860 nm. It also represents the evident correspondence between the data points for: (A) the SERS intensities (shown in an ascending trend as blue dots followed by black arrows) and (B) corrected absorbance for λ_{MAX} (shown in a descending trend as red dots followed by red arrows) that were adapted in this study.

PART NINE: CONCLUSION

The Au@Ag system was analyzed via μ-titrations using SERS labels and under different concentrations of KCl. Evidently, the enhanced SERS that was obtained from the application of the three analytes of: R6G, MPY and MBA had adsorbed to the monomeric Au@Ag nanoparticles. The difficult aspects of the calibration of SERS signals, which were addressed from the present application, appeared to support previous results for the SERS label of MBA. Overall, the data here reported consistently showed that as soon as an aggregate event was reached, an enhanced SERS signal followed through. This conclusion is fully supported, by the detailed optical analysis of the SERS intensity versus the aggregate extinction, and it also accounts approximately for the absorption in all solutions. The signal intensities along the slope of the calibration curve (positive and sometimes even negative) were affected drastically by the order of addition of the aggregant KCl. In contrast to the aggregation of monomeric NPs that had been initiated only with addition of SERS label; the aggregation state was not only extended but it appeared more pronounced i.e., from evidence of stronger SERS signals as soon as the Au@Ag NPs were treated with KCl.

While graphical representations of the integral of the SERS intensities versus the Au@Ag aggregate extinctions showed a highly linear correlation for R6G-first-KCl runs; the order of addition for KCl-first-R6G exhibited an abrupt onset right before the Au@Ag aggregations became evident.

The data for the KCl-First-MBA SERS intensities during the [MBA] runs were the least revealing because even when the peak SERS intensities appeared at the lowest

[MBA] these were followed by a steadily signal declined, even after more KCl had been added. Nonetheless, this trend depicted a gradual aggregation during the KCl-first-MPY additions but did not appear as conclusive as those from R6G-First-KCl and MPY-First-KCl.

To determine the next project to this one, it would be advisable to start with the analysis of MPY therefore, a clear distinction of the onset trend could be used to quickly discern between what setting to apply for label and KCl additions. This approach saved a lot of time in the setting of more micro-titrations that were used in this project.

Lastly, in terms of the slope and range of the evidently SERS onset, the MBA-first-KCl titrations that resembled those from KCl-first-R6G and KCl-first-MPY only occurred at about a 10% of a total potential magnitude. It is also relevant to note that irrespective of [MBA] the signals rose quickly at about 20 mM KCl and they tracked the aggregate band almost exactly as it became a flat trend, thereafter. No significant trends were seen in the KCl-first-MBA titrations that resembled the titrations of R6G and MPY. Limiting the observations to the label-first cases, however, the label concentration did not matter in generating the largest SERS signals. Over the range of label concentrations studied, the maximum signal was achieved independently of label concentration, but they peaked at a high KCl concentration between 2-5 mM. This interesting result suggests that the phenomenon as studied is limited by the number of nanoparticle aggregates that can form, as opposed to the amount of label that was added. Based on these extensive titrimetric studies, a further study of this fascinating problem is clearly needed by designing newer targeted aggregations that could aid in the discovery of the mechanisms that underlie the enhancement of SERS around similar systems like that of Au@Ag NPs.

LITERATURE CITED

1.   Strutt, J..*Philosophical Magazine* **1871**, *4* (41), 447-454.

2.   Raman, C. V..*Proc. Roy. Soc. London A* **1922**, *101*:64.

3.   Smith, E.; and Dent, G. *Modern Raman Spectroscopy – A Practical Approach*; Wiley: England, 2005.

4.   Grasselli, J. G.; Snavely, M. K.; and Bulkin, B. J. *Chemical Applications of Raman Spectroscopy*; Wiley: N.Y., 1981, 4-137.

5.   Andrews, D. L.; and Demidov, A. A. *An Introduction to Laser Spectroscopy*; Springer: N.Y., 2002; 77.

6.   Jayaraman, A.; Ramdas, A. K. Chandrasekhara Venkata Raman. *Phys. Today* **1988**, *41*:8, 56.

7.   Lewis, I. R.; and Edwards, H. *Handbook of Raman Spectroscopy: From the Research Laboratory to the Process Line*; Marcel Dekker, Inc., 2001.

8.   Smekal, A. *Naturwissenchaften* 1923, *43*, 873.

9.   Kramers, H.A.; Heisenberg, W. *Z. Phys.* **1925**, *31*, 681.

10.   Schrodinger, E. *Ann. Phys.* **1926**, *81*:109.

11.   Raman, C.V.; and Krishnan, K. S. *Nature* 1928, *121,* 501.

12.   Raman, C.V.; Krishnan, K.S. *Proc. Roy. Soc. London* 1929, *122*, 23.

13.   Kasha, M.; and Oppenheimer, Jr. (transl) Davydov, A. S. *Theory of Molecular Exciton;* McGraw-Hill, N. Y., 1962.

14.   Lommel, E. *Wiedemann's Ann. D. Phys.* **1878**, *3*:251.

15.   Landsberg, G.S.; and Mandelstam, L. I. *Natural Science* **1928**, *16*, 557.

16.   Brillouin, L. *Ann. Phys.* 1922, *88*, 17.

17.   Jayasooriya, U. A.; Jenkins, R. D. *Introduction to Raman Spectroscopy*; School of Chemical Science - Springer, U.K. 2002.

18.   Long, D. *The Raman Effect: A Unified Treatment of the Theory on Raman Scattering by Molecules*; Wiley: N.Y., 1977.

19.   Ferraro, J. R.; Nakamoto, K. *Introductory Raman Spectroscopy*; Academy Press, San Diego, 1994.

20.   Clark, R.J.H.; Dines, T.J. *Agnew. Chem., Int. Ed. Engl*. **1986,** *27*, 131–158.

21.   Clark, R.J.H.; Dines, T.J. *Mol. Phys.*, **1982**, *45*, 1153.

22.   Atkins, P.; de Paula, J. *Atkins' Physical Chemistry*; W. H. Freeman and Co., N. Y., eighth edition, 2006.

23.   Long, D. A.; *The Raman Effect: A Unified Treatment of the Theory of Raman Scattering*; Wiley, N. Y., 2001.

24.   Rousseau, D. L.; Friedman, J.M.; Williams, P.F. *Topics in Current Physics*; Springer, N.Y., 1979.

25.   Banwell, C. N.; McCash, E. M. *Fundamentals of Molecular Spectroscopy*; McGraw-Hill, 1994.

26.   Schrader, B.; Dipple, B.; Erb, I; Keller, S.; Lochte, T.; Schultz, H. Tatsch, E.; Wessel, S. *J. Mol. Struct.*, **1999**, *480-481*, 21.

27.   Fadini, A.; Schnepel, F. –M. *Vibrational Spectroscopy: Methods and Applications*; Ellis Horwood Ltd, Chichester, 1989.

28.   Colthrup, N. B.; Daly, L. H.; Wiberley, S. E. *Introduction to Infrared and Raman Spectroscopy*; Academic Press, San Diego, 1990.

29.   Jones, H. C.; Warnes, G. *FT Raman Spectroscopy*; Ellis Horwood Ltd, 1991.

30.   Lin-Vien, D.; Colthrup, C. B.; Fateley, W. G.; Grasselli, J. G. *The Handbook of Infrared and Raman Characteristic Frequencies of Organic Molecules*; Wiley, N. Y., 1991.

31.   Laserna, J.J. *Modern Techniques in Raman Spectroscopy*; Wiley, 1996.

32.   Hendra, P.; Jones, C.; Warnes, G. *Fourier Transform Raman Spectroscopy*; Ellis Horwood Ltd., 1991.

33.   Shi, H.; Chen, S-Y.; Lin, K. *W.J.G.E.* **2016**, *8*(5), 273-275.

34.   Willets, K. A.; Van Duyne, R. P. *Annu. Rev. Phys. Chem.* **2007**, *58*, 267-297.

35.   Fleischmann, M.; Hendra, P. J.; McQuillan, A. J. *Chemical Physics Letters*. **1974**, *26*(2), 163-166.

36.   Jeanmarie, D. C.; Van Duyne, R. P. *J. Electroananlytical Chem.* **1977**, *84*, 1-20.

37.   King, F. W.; Van Duyne, R. P.; Schatz, G. C. *J. Chem. Phys.* **1978**, 69, 4472–4481.

38.   Albrecht, M. G.; Creighton, J. A. *J. Am. Chem. Soc.* **1977**, *99*(15), 5215-5217.

39.   Kneipp, K.; Wang, Y.; Kneipp, H.; Perelman, L. T.; Itzkan, I.; Dasari R. R.; Feld, M. S. *Physical Review Letters*. **1978**, *78*, 1667–1670.

40.   Nie, S.; Emory, S. R. *Science*. **1997**, *275*, 1102–1106.

41. Le Ru, E. C.; Meyer, M.; Etchegoin, P. G. *Journal of Physical Chemistry B* **2006**, *110*, 1944–1948.

42. Liu, B.; Han, G; Zhang, Z.; Liu, R.; Jiang, Ch.; Wang, S.; Han, M-Y. *Analyt. Chem.* **2012**, *84*, 255-261.

43. Liu, B.; Zhou, P.; Liu, X.; Sun, X.; Li, H.; Lin, M. *Food Bioprocess Technology*. **2013**, *6*, 710-718.

44. Dasary, S. S. R.; Jones, Y. K.; Barnes, S. L.; Ray, P. C.; Singh, A. K. *Sensors and Actuators*. **2016**, *224,* 65-72.

45. Yang, Sh.; Dai, X.; Boschitsch Stogin, B.; Wong, T-S. *PNAS*. **2016**, *113*(2), 268-273.

46. Israelen, N. D.; Wooley, D.; Hanson, C.; Vargis, E. *Journal of Biological Engineering,* **2016**. *10*(2), 1-12.

47. Samal, A. K.; Polavarapu, L.; Rodal-Cedeira, S.; Liz-Marzán, L. M.; Pérez-Juste, J.; Pastoriza-Santos, I. *Langmuir*. **2013**. *29*, 15076-15082.

48. Moskovits, M. *Reviews on Modern Physics*. 1985, *57*(3), 783-828.

49. McFarland, A.D.; Young, M.A.; Dieringer, J.A.; Van Duyne, R.P. *J. Phys. Chem. B* **2005,** *109*:11279–85.

50. Hoff, Christopher, *MS Thesis*, San Jose State University, 2013.

51. Bhatia, P.; Consiglio, J.; Diniz, J.; Lu, J. E.; Hoff, CH.; Ritz-Schubert, S.; Terrill, R. *Journal of Spectroscopy* **2015,** *2015*, 1.

52. Kimling, J.; Maier, M.; Okenve, B.; Kotaidis, V.; Ballot, H.; Plech, A. *The Journal of Physical Chemistry B* **2006***, 110*, 15700-15707.

53. Horvath, H.; Mie, G. *J. Quant. Spect. and Radiat. Transf.* **2009**, *110*, 787-799.

54. Johnson, P.; Christy, R. *Phys Rev B* **1972**, *6*:4370–4379.

55. Lu, W.; Arumugam, S.R.; Senapati, D; Singh, A.K.; Arbneshi, T; Khan, S.A.; Yu, H. *ACS Nano* **2010**, *4*, 1739–1749.

56. Xie, W.; Su, L.; Shen, A.; Materny, A.; Hu, J. *J. Raman Spec.* **2011**, *42*, 1248–1254.

57. Mayer, K. M.; Hafner, J. H. *Chem. Rev.* **2011**, *111*, 3828–57.

58. Xu, W.; Xue, X.; Li, T.; Zeng, H.; Liu, X. Angewandte Chemie (International ed. in English) **2009**, *48,* 6849–52.

59. Amendola, V.; Bakr, O. M.; Stellacci, F. *Plasmonics* **2010***, 5*, 85-97.

60.   Bengter, H.; Tengroth, C.; Jacobsson, S. P. *J. Raman Spectrosc.* **2005***, 36*, 1015-1022.

61.   Kitching, H.; Kenyon, A.; Parkin, I. *Physical Chemistry Chemical Physics* **2014***, 16*, 6050-6059.

62.   Mihailescu, G.; Olenic, L.; Pruneanu, S.; Bratu, I.; Kacso, I. *Journal of optoelectronics and advanced materials* **2007***, 9*, 756-759.

63.   Fraire, J. C.; Pérez, L. A.; Coronado, E. A. *The Journal of Physical Chemistry C* **2013***, 117*, 23090-23107.

64.   Jain, P. K.; Lee, K. S.; El-Sayed, I. H.; El-Sayed, M. A. *The Journal of Physical Chemistry B* **2006***, 110*, 7238-7248.

65.   Cortie, M. B.; McDonagh, A. M. *Chemical reviews* **2011**, *111*, 3713–35.

66.   Campion, A.; Kambhampati, P. *Chem. Soc. Rev.* **1998***, 27*, 241-250.

67.   Lombardi, J. R.; Birke, R. L. The Journal of Physical Chemistry C **2008**, 112, 5605-5617.

68.   Orendorff, C. J.; Gole, A.; Sau, T. K.; Murphy, C. J. *Anal. Chem.* **2005***, 77*, 3261-3266.

69.   Link, S.; El-Sayed, M.A. *J. Phys. Chem. B*, **1999**, *103*, 8410-8426.

70.   Freitag, I.; Neugebauer, U.; Csaki, A.; Fritzsche, W.; Krafft, C.; Popp, J. *Vibrational Spectroscopy* **2012***, 60*, 79-84.

71.   Jain, P.; Lee, K.S.; El-Sayed, I.H.; El-Sayed, M.A. *J. Phys. Chem. B.* **2006**, *110*, 7238-7248.

72.   Creighton, J.A. *Spectroscopy of Surfaces*; (Clark, R. J. H.; Hester, R. E. eds.); Wiley, N.Y. 1998, 27.

73.   Otto, A.; Mrozek, I. Grabhorn, H. Akeman, W. *J. Phys. Cond. Matt.* **1992**, *4*, 1143-1212.

74.   Wustholz, K. L.; Henry, A.; McMahon, J. M.; Freeman, R. G.; Valley, N.; Piotti, M. E.; Natan, M. J.; Schatz, G. C.; Duyne, R. P. V. *J. Am. Chem. Soc.* **2010***, 132*, 10903-10910.

75.   Kleinman, S. L.; Sharma, B.; Blaber, M. G.; Henry, A.; Valley, N.; Freeman, R. G.; Natan, M. J.; Schatz, G. C.; Van Duyne, R. P. *J. Am. Chem. Soc.* **2013***, 135*, 301-308.

76.   Braun, G. B.; Lee, S. J.; Laurence, T.; Fera, N.; Fabris, L.; Bazan, G. C.; Moskovits, M.; Reich, N. O. *J. Phys. Chem. C* **2009***, 113*, 13622-13629.

77. Henry, A.; Bingham, J. M.; Ringe, E.; Marks, L. D.; Schatz, G. C.; Van, D., Richard P. *J. Phys. Chem. C* **2011**, *115*, 9291-9305.

78. Schatz, G. C. Acc. Chem. Res. **1984**, 17, 370.

79. McCall, S.; Platzman, P.; Wolff, P. Phys. Lett. A **1980**, 77, 381.

80. Zeman, E. J.; Schatz, G. C. J. Phys. Chem. **1987**, 91, 634.

81. Pristinski, D.; Tan, S.; Erol, M.; Du, H.; Sukhishvili, S. *J. Raman Spectrosc*. **2006**, 37, 762-770.

82. Ghosh, S. K.; Pal, T. *Chem. Rev*. **2007**, 107, 4797-4862.

83. Otto, A. *J. Raman Spectrosc*. **2005**, 36, 497-509.

84. Moskovits, M. *J. Raman Spectrosc.* **2005**, 36, 485-496.

85. Stiles, P. L.; Dieringer, J. A.; Shah, N. C.; Van Duyne, R. P. *Annu.Rev.Anal.Chem.* **2008**, *1*, 601-626.

86. Michaels, A. M.; Nirmal, M.; Brus, L. E. *J. Am. Chem. Soc.* **1999**, *121*, 9932-9939.

87. Morton, S. M.; Silverstein, D. W.; Jensen, L. *Chemical reviews* **2011**, *111*, 3962–94.

88. Derjaguin, B.; Landau, L. D. *Acta Phys. Chim*. **1941**, *14*, 633-662

89. Ravina, L.; Moramarco, N. Everything You Want to Know About Coagulation and Flocculation. Zeta-Meter, Inc. Fourth ed. **1993**, 10-12.

90. Verwey, E. J. W.; Overbeek, J. T. G. Theory of Stability of Lyophobic Colloids. *Elsevier*, **1948**.

91. Elimelech, M.; Gregory, J.; Jia, X.; Williams, R. *Particle Deposition and Aggregation: Measurement, Modeling, and Simulation.* Butterworth-Heinemann Ltd. Oxford, 1995.

92. Kitching, H.; Kenyon, A.; Parkin, I. *Physical Chemistry Chemical Physics* **2014**, *16*, 6050-6059.

93. Mulvaney, P. In *Metal Nanoparticles: Double Layers, Optical Properties, and Electrochemistry;* Nanoscale Materials in Chemistry; John Wiley & Sons, Inc.: **2001**; pp 121-167.

94. Bockris, J. O.; Reddy, A. K. In *Modern electrochemistry: an introduction to an interdisciplinary area;* Springer: **1973**; Vol. 2.

95. Wang, Y.; Hu, H.; Jing, S.; Wang, Y.; Sun, Z.; Zhao, B.; Zhao, C.; Lombardi, J. R. *Analytical Sciences* **2007**, *23*, 787.

96.   Xia, L.; Jia, Y.; Liu, G.; Yang, Z.; Chen, X.; Zhang, H.; Sun, M. *J. Raman Spectrosc.* **2010***, 41*, 398-405.

97.   Le Ru, E.; Blackie, E.; Meyer, M.; Etchegoin, P. *J. Phys. Chem. C* **2007***, 111*, 13794-13803.

98.   Dudik, J. M.; Johnson, C. R.; Asher, S. A. *J. Chem. Phys.* **1985***, 82*, 1732-1740.

99.   Pristinski, D.; Tan, S.; Erol, M.; Du, H.; Sukhishvili, S. *J. Raman Spectrosc.* **2006***, 37*, 762-770.

100.   Holler, F. J.; Skoog, D. A.; Crouch, S. R. Principles of Instrumental Analysis; Cole Publishing: Pacific Grove, USA: **2007**.

101.   Stiles, P. L.; Dieringer, J. A.; Shah, N. C.; Van Duyne, R. P. *Annu. Rev. Anal. Chem.* **2008***, 1*, 601-626.